High-resolution grids of daily air temperature for Peru - the new PISCOt v1.2 dataset

Adrian Huerta[1,2,*], **Cesar Aybar**[3], **Noemi Imfeld**[4,5], **Kris Correa**[1], **Oscar Felipe-Obando**[1], **Pedro Rau**[6], **Fabian Drenkhan**[7], **and Waldo Lavado-Casimiro**[1]

[1]Servicio Nacional de Meteorología e Hidrología (SENAMHI), Lima, Perú.
[2]Departamento de Física y Meteorología, Universidad Nacional Agraria La Molina (UNALM), Lima, Perú
[3]Department of Geoinformatics – Z_GIS, University of Salzburg, Austria
[4]Institute of Geography, University of Bern, Bern, Switzerland
[5]Oeschger Centre for Climate Change Research, University of Bern, Bern, Switzerland
[6]Centro de Investigación y Tecnología del Agua (CITA), Departamento de Ingeniería Ambiental, Universidad de Ingeniería y Tecnología (UTEC), Lima, Perú
[7]Geography and the Environment, Department of Humanities, Pontificia Universidad Católica del Perú, Lima, Peru
[*]corresponding author(s): Adrian Huerta (adrhuerta@gmail.com)

ABSTRACT

This study describes the development of PISCOt (v1.2), an innovative high-spatial resolution (0.01°) daily air temperature dataset for Peru (1981-2020). The development of PISCOt involves four main steps: i) quality control; ii) gap-filling; iii) homogenisation of weather stations; and iv) spatial interpolation. The methodological framework allows the representation of the complex spatial variability of air temperature at a more accurate scale than other national and global products (e.g. PISCOt v1.1, ERA5-Land, TerraClimate, CHIRTS). The technical validation indicates mean absolute errors of less than 1.5 °C at climatological and daily mean scales. The new PISCOt dataset appropriately captures the temporal trends which highlights its usefulness to understand the historical variability of air temperature. For the first time, PISCOt v1.2 provides a suitable and widely applicable baseline at the local and regional level in the face of data scarcity in several regions of Peru for applications related to climate change, water balance studies, or the assessment of ecosystems, among others.

Background & Summary

Air temperature is a fundamental parameter of the climate system, which is required for various applications such as ecology[1], hydrology[2], public health[3], agriculture[4], climate variability, and climate change[5,6]. Typically, temperature values are obtained from meteorological stations and show high accuracy and temporal resolution but do not capture information for an entire unit or region of analysis. Therefore, global- or continental-scale gridded databases, derived from interpolated[7], reanalyzed[8] and/or combined[9] in-situ and surface remote sensing data, are widely used. While each dataset offers several advantages for specific applications, limitations related to complex topography, spatial resolution, and the amount of assimilated data reduce their reliability[10,11]. In recent years, high-resolution gridded climate datasets at national and sub-national scales has been produced to close this gap[12–18].

Various methods exist for creating gridded air temperature data based on weather stations. Traditionally, they have been divided into geostatistical, non-geostatistical, and combined methods[19,20]. Although these methods are widely used and provide high efficiency, more recent procedures based on artificial intelligence[21,22] and machine learning[23,24] are gaining relevance due to their ability to work with large amounts of data and capture non-linear and multivariate relationships[25]. However, the reduced capacity to estimate the value outside the range of the training data limits its use in large regions with low station density[26,27]. Besides, since the relationship between air temperature and auxiliary spatial predictors varies on spatiotemporal scales, recent research has also highlighted the importance of non-stationarity in the spatiotemporal domain by building local models in contrast to global estimation models[13,28–32]. The diversity of methods has advantages and disadvantages regarding data availability, computational efficiency, computational cost, and estimation accuracy. Therefore, the method selected must be suitable or at least adapted to the purpose and area of study.

In South America, only few efforts have been undertaken to create gridded temperature datasets, mainly because of the low density of weather stations or the lack of long-term data series. However, there are significant advances in the construction of gridded datasets in countries such as Brazil[33,34], Chile[35], and Bolivia[36,37]. For Peru, two first databases exist. The (1) is a monthly-scale gridded product for 1964–2014 at 5 km spatial resolution (henceforth "VS2018") developed by Vicente-Serrano[38]. The (2) is a daily-scale gridded product for 1981–2016 at 10 km spatial developed by the National Service of Meteorology and Hydrology (SENAMHI). SENAMHI establishes this product as part of the Peruvian interpolated data of the Climatological and Hydrological Observations of SENAMHI (PISCO), denominated PISCOt v1.1[39]. Since its release, PISCOt has been applied in numerous areas of research and operation[3,40–45]. Due to the increasing availability of observed data and the need for higher spatial resolution, it is crucial to build a new gridded air temperature product that allows modelling and understanding processes at local scales, e.g., at the catchment level. Previously applied techniques show that the product can be optimised by enhancing the temporal homogeneity of the observed data and also by using topographic and climatic co-variables. Among the applied remote sensing data, Land Surface Temperature (LST) is the most frequently used parameter because it improves both the numerical accuracy and the spatiotemporal details of the interpolated air temperature[46–49].

Here, we present an updated version (v1.2) of PISCOt consisting of a daily gridded dataset for maximum (Tmax) and minimum (Tmin) air temperature at a spatial resolution of 0.01° ($\sim$1 km) for the period 1981–2020. The updated version of PISCOt is essential for two main reasons: i) it provides high-resolution estimates of daily Tmax and Tmin in a data scarce region with complex topography, resulting in high uncertainty for estimating the local temperature; and ii) it provides the basis for further applications such as studies related to climate change analysis, hydrological modeling, and ecology, among others.

Methods

Workflow for generation of the data

Missing, inhomogeneous, and non-quality-controlled data are a typical concern in hydro-climatology-related studies. Especially in countries with low financial resources and limited technical capacities: weather station networks are often sparse with poor coverage in rural and remote areas, many stations do not work appropriately, and quality control systems are inefficient[50,51]. In Peru, quality issues with station data are especially challenging due to the complex topography leading to steep climatic gradients[52,53]. The development of PISCOt requires therefore a pre-processing of the station observations before spatial interpolation is applied.

The workflow for the development of the datasets consisted of four steps: i) quality control, ii) gap-filling, iii) homogenisation, and iv) spatial interpolation (Fig. 1). In step i), statistical and visual techniques were applied to remove erroneous data in the times series of Tmax and Tmin. In ii), the time series were gap-filled using data from neighbouring stations. The previously gap-filled data were then homogenised in step iii) to reduce temporal inhomogeneities. Once a complete and homogenised database of Tmax and Tmin observations was established, we proceeded to step iv). A climatologically based interpolation approach[54–57] was used, where the spatial interpolation was divided into the mean monthly normal and anomalies and then aggregated to obtain the final product. Topographic and remote sensing data served as a basis to estimate air temperature at the country scale. The following sections present the data sources and the four development steps in more detail.

Weather station data

Data source

The database used in this study belongs to SENAMHI and includes 430 daily series of Tmax and Tmin (Fig. 2). To obtain a better spatial representation of the country boundaries (Fig. 2a), also data from the meteorological services of Bolivia (3 time series), Brazil (5), Chile (3), Colombia (3), and Ecuador (18) were used leading to a total of 462 potential time series (Fig. 2b).

The spatial distribution of the stations was highly uneven in the study area. Specifically, in the Amazon region, there was a significant shortage of stations. Station density was higher mainly in the Andes and particularly at the Pacific Coast (Fig. 2). Depending on the altitude, there was a lower (higher) density of stations between 1000 and 2000 masl (0–1000 masl and $>$ 3000 masl)[58]. Thus, the spatial distance between stations varied considerably. The earliest observations started in the 1930s, with a significant increase up to date. Due to political instability and social conflicts (Supplementary Fig. 1), two episodes of under-reporting occurred before 1960 and during the 1980s. Due to the low reliability of data before the 1980s, the gridded product only covered the period 1981 to 2020. Also, only stations with at least five years of data (365 days of the year repeated at least five times) were used. The 5-year threshold was chosen based on the finding that at least 5-7 years of observations are required before pairwise relationships between stations stabilise[13,59,60].

Quality control

The quality control (QC) of the air temperature series comprised the following steps:

1. Obvious errors: conversion of numerical values (-999, -99.9, -88.8) to empty values, and removal of duplicate or incorrectly formatted dates.

2. Extreme values: flagging of extreme (low and high) air temperature values based on physical and statistical values. The physical maximum and minimum limits for Tmax (Tmin) were 60 °C and -10 °C (40 °C and -30 °C), respectively[61]. The statistical algorithm identified records that are above or below the 3rd (1st) quartile plus or minus *m* times the interquartile range (IRQ). For Tmax and Tmin, *m* was set to 3.5.

3. Internal consistency: inspection of records where Tmax is below Tmin. Also, values where flagged, when Tmax and Tmin had the same magnitude (Tmax = Tmin).

4. Temporal coherence: inspection of values repeated over a long period and very extreme (day-to-day) jumps. It was defined that a value can be the same up to a maximum of 8 days. In addition, a daily jump may not have a variation over 20 °C[62].

5. Spatial coherence: inspection of the daily percentile series of a target station with up to four neighbouring stations. A neighbouring stations was defined as lying within a radius of 70 km and an altitudianl range of 500 m with respect to the target station. The records of the target station with differences greater than 0.85 concerning the average of the neighbouring stations were

identified. The percentile difference approach allows for identifying only the most extreme spatial variations[63–66].

6. Visual inspection: a visual inspection of the time series was carried out to identify periods with inhomogeneities that cannot be corrected (rounding errors, asymmetric rounding patterns, measurement precision, time irregularities, and obvious inhomogeneities)[51,67]. For this purpose, we used daily series and annual decimal frequency charts.

All QC-flagged values were set as a missing observation after the QC steps (Supplementary Fig. 1 and 2). For the following procedures, only stations that retained the 5-year threshold after the QC were used. In addition, we manually verified the elevation information of weather stations using a digital elevation model and modified it where necessary.

Gap-filling

Simple interpolation of incomplete data may produce artificial inhomogeneities in the gridded product due to the irregular spatiotemporal distribution of weather stations during the 1981–2020 period[68,69]. This can affect the variance and lead to erroneous conclusions on changes and variability[70]. To reduce such artifical inhomogeneities, data reconstruction of time series that do not cover the entire period and of gaps within time series was necessary.

A gap-filling procedure based on neighbouring stations[71] was implemented to create a complete database. Before applying the algorithm, the available information was standardised using a daily climatology of the available data to avoid differences in the mean and the variance[72]. Subsequently, the model estimates were corrected to approximate the observed values as closely as possible. The correction was made by applying empirical quantile mapping[73,74]. The Tmax and Tmin series were reconstructed independently.

A neighbouring station was considered for gap-filling if it met two conditions: (i) at least five years of data in common, and (ii) a correlation greater than or equal to 0.6 with the target station. An iterative process of the gap-filling algorithm was performed to take advantage of those stations that did not have a common period at the beginning[75]. This was carried out in up to three iterations, where the availability of neighbouring stations was limited according to the following characteristics: horizontal-vertical distances of i) 70 km–500 m, (ii) 100 km–500 m, and (iii) 150 km (no vertical limit), respectively. A maximum of 8 neighbouring stations was considered during this procedure. The rationale for this configuration was based on a previous correlation-distance-elevation analysis (Supplementary Fig. 3).

Due to the low density of weather stations in some regions, virtual stations (time series at the closest grid point) from the ERA-5 Land reanalysis[76] were additionally included to fill temporal gaps. These time series were not directly used, but an anomaly-based bias correction (de-trended empirical quantile mapping[77]) was applied to series with at least ten years of data. Only those virtual stations with a correlation greater than or equal to 0.6 with the target station (within Peru) were preserved and used for gap-filling.

Homogenisation

Many non-climatic influences can affect measurements (changes in station location, instrumentation, and observing practices, among others). To eliminate these inhomogeneities and to obtain a more reliable observations, time series must be homogenised[78,79]. A variety of statistical methods has been developed, each with different results[78,80]. In sparse networks, homogenisation performance is drastically reduced, and there is a risk of erroneous corrections due to the low signal-to-noise ratio[81]. Consequently, the chosen method must be applied carefully.

We tested the temporal homogeneity using the Standard Normal Homogeneity Test[82,83] in its relative (Pairwise Homogeneity Algorithm (PHA)[84,85]) and absolute implementation. The process was fully automatic and straightforward. Therefore, the approach was objective, unlike semi-automatic approaches that require several subjective decisions that can influence the whole process[67]. In addition, PHA has been applied at global scale datasets[86,87], and is one of the approaches with the best performance[78,80].

The algorithm searched a maximum (minimum) of eight (four) neighbouring reference stations with a correlation greater than or equal to 0.6 with the target station within a horizontal (vertical) distance of 1000 km (1000 m) in order to perform a relative test. In absence of these conditions, the absolute test was applied. Absolute tests have a lower detection efficiency than relative tests[78]. Therefore, the condition was designed as a backup test when a relative test was almost impossible to apply[88]. In both cases, a p-value < 0.05 (with a 95% confidence interval) was used to define significant breakpoints which were then used to adjust past values compared to the present.

As the algorithm was applied on a monthly scale, a linear time interpolation of the monthly correction factors to a daily scale was performed[89]. The homogeneity tests were applied after the gap-filling to i) detect inhomogeneities introduced by the gap-filling process and ii) because the process was more reliable if the time series had no gaps[50,64]. Finally, as for the gap-filling procedure, homogenisation was performed in up to three repetitive cycles according to the boundary conditions previously defined.

Spatial predictors for air temperature

In the gridding process, Tmax and Tmin were adjusted to a series of auxiliary spatial predictors such as land surface temperature (LST), elevation (DEM), latitude (Y), longitude (X), and the topographic dissection index (TDI).

The LST observations came from the MODIS database[90]. The product had an average time scale of 8 days starting in 2000 and a spatial resolution of 1 km. The Terra version (MOD11A2 V6)[91] was used for day (LST_day) and night (LST_night) times. Because of missing data before 2000, the average monthly values for 2000-2020 for both day and night times were used as spatial predictors for Tmax and Tmin, respectively. Only LST values were used without cloud contamination, emissivity error > 0.02, or LST errors > 2 °C. If any pixels in the final average were empty, they were reconstructed through nearest neighbour interpolation. The LST was downloaded from https://developers.google.com/earth-engine/datasets/catalog/MODIS_006_MOD11A2 (accessed 31 October 2022).

The DEM data were obtained from the Global Multi-resolution Terrain Elevation Data (GMTED) 2010[92] at a spatial resolution of 1 km. This dataset was selected because it has also been used in other temperature-gridded products at a national level[38]. X, Y, and TDI were derived at the same spatial resolution as the DEM. The digital elevation model was downloaded from https://developers.google.com/earth-engine/datasets/catalog/USGS_GMTED2010 (accessed 31 October 2022).

The TDI was calculated through a multi-scale DEM calculation:

$$TDI_{(s_0)} = \sum_{i=1}^{n} \frac{Z(s_0) - Z_{min}(i)}{Z_{max} - Z_{min}(i)} \tag{1}$$

Where $TDI_{(s_0)}$ is the final multi-scale TDI value for the grid cell location s_0, $Z(s_0)$ is the elevation at the grid cell location s_0, $Z_{min}(i)$ is the minimum elevation at the grid cell location in the spatial window i, $Z_{max}(i)$ is the maximum elevation at the grid cell location in the spatial window i, and n is the number of spatial windows[93]. The TDI value for a specific window size represented the height of a grid cell relative to the surrounding terrain. The multi-scale TDI was calculated for five spatial window sizes (at 3, 6, 9, 12, and 15 km). Valley bottoms and low areas relative to surrounding grids have values close to zero, while ridges and areas above surrounding areas have high values approaching 5. The selection of this topographic variable was based on the high correlation with daily Tmin anomalies which are influenced by cold air drainage[13,93].

The spatial predictors were downloaded from the Earth Engine Data Catalog[94] repository via rgee[95]. For efficient processing, the data were brought to the extent of -81.405°, -67.185°, -18.595°, and 1.225° (min longitude, max longitude, min latitude, and max latitude); and re-gridded to 0.01°, corresponding to the resolution of the final product.

Air temperature interpolation

For the interpolation of Tmax and Tmin, a climatologically aided interpolation (CAI) approach[54–57] was used, which combines long-term climate information with daily station data to obtain field estimates on shorter time scales. This allowed the dissemination of information from weather patterns to daily fields. With CAI, deviations from the average (anomalies) on a given day were interpolated and combined with an average field (climatology) to produce the final daily product. The CAI approach has been employed in several studies[13,18,57,66]. It has proven to be effective in improving the accuracy of air temperature estimation in regions of complex terrain with limited observations[96–99]. This approach drastically reduced computational costs (compared to applying it independently for each time step), and the co-variables did not necessarily need to be in the same temporal range as the observational data. The procedure was applied independently for Tmax and Tmin and comprised three steps:

1. Interpolation at monthly (normal) average scale (1981-2010)
2. Interpolation at the daily anomaly scale (based on the monthly normal) for the 1981–2020 period
3. Combination of 1 and 2 to obtain the daily temperature value.

Monthly normal interpolation

For the interpolation of the monthly normal, the Regression-Kriging (RK) method[13,100,101] was used, which represents a spatial process expressed as the sum of a deterministic and a stochastic part:

$$\overline{T}(s_0,m_0) = \overline{T}_u(s_0,m_0) + \overline{T}_e(s_0,m_0) \tag{2}$$

Where $\overline{T}(s_0,m_0)$ is the final interpolated normal temperature at the grid cell location s_0 and for the month m_0, $\overline{T}_u(s_0,m_0)$ is the deterministic spatial trend in normal temperature modelled by the weather station locations and auxiliary predictors, and $\overline{T}_e(s_o,m_o)$ is the spatially autocorrelated stochastic residual with zero mean[102]. We use a linear model to fit $\overline{T}_u(s_0,m_0)$, and ordinary kriging (OK) to interpolate the residual part $\overline{T}_e(s_o,m_o)$:

$$\overline{T}(s_0,m_0) = \beta_0 + \beta_1 lst(m_0) + \beta_2 z + \beta_3 x + \beta_4 y + \sum_{i=1}^{n} w_i(s_0,m_0)\overline{T}_e(s_i,m_0) \tag{3}$$

β_0 is the intercept; β_1, β_2 β_3 and β_4 are the model coefficient estimates for monthly average LST, elevation, latitude, and longitude, respectively; $lst(m_0)$, z, x and y are the average LST at m_0, elevation, longitude, and latitude at grid level at the location s_0; $w_i(s_0,m_0)$ are the weights defined by the residual spatial covariance; and $\overline{T}_e(s_i,m_0)$ are the residuals of the regression for n stations.

Due to the large variability and extent of the study area, it was not appropriate to use a global model for the spatial prediction of normal temperature. A version of RK with a moving spatial window based on Geographically Weighted Regression-Kriging (GWRK)[103] was used to account for the spatial heterogeneity in the interpolation process. The GWR[104,105] calculated local trends for a subset of the study area with a weighting of weather stations using a distance-based function. To improve prediction accuracy, it added the OK from the residuals to the regression estimate. The weighting of the observations in GWR was calculated using the bi-square kernel nearest neighbourhood function:

$$w_i(s_0) = \left[1 - \left(\frac{h(s_0)_i}{r}\right)^2\right]^2 \tag{4}$$

Where $w_i(s_0)$ is the distance-based weighting function of the station i at the interpolation location s_0, $h(s_0)$ is the distance between the station i and the interpolation location s_0, r is the bandwidth for the size of the spatially adaptive kernel function. The bandwidth optimisation was necessary because a significant deviation in estimating the regression parameters would be generated if the bandwidth were too large or too small[104]. The Corrected Akaike Information Criterion automatically determined the optimal bandwidth[105].

The GWR coefficients were estimated at a spatial resolution of 0.1°, assuming that the relationship between the normal temperature and the auxiliary predictors is independent of the spatial resolution scale[106,107]. Then it was locally interpolated with a bilinear approach at a resolution of 0.01° to be applied to the auxiliary predictors. The OK of the residuals was set to 0.05° and then disaggregated to 0.01° to reduce the measurement precision inconsistencies[51,108,109] of the observed time series (Supplementary Fig. 4). Both sub-products at the final resolution were aggregated according to Equation 3 to obtain the grids of the monthly normals of Tmax and Tmin.

We used the GWmodel[105] and gstat[110,111] packages for the implementation of GWRK. For the estimation of the theoretical variogram (in OK), an automatic adjustment by iteratively repeated minimum squares was used, and the nugget value was forced to zero according to the automap package[112].

Daily interpolation

A method similar to the monthly normal temperature was used in the daily temperature interpolation. In this sense, the daily anomalies of Tmax and Tmin were expressed as the sum of two components (deterministic and stochastic). Because of the large number of days (14244) per variable and the intention to produce PISCOt operationally, it was chosen to use RK due to computational limitations. The model here was similar to Equation 3 but added the spatial predictor TDI.

Therefore, the daily temperature product was obtained according to:

$$T(s_0,d_0) = \overline{T}(s_0,m_0) + \delta T(s_0,d_0) \tag{5}$$

Where $T(s_0,d_0)$ is the temperature at the interpolation point s_0 for the day d_0 within the month m_0, $\overline{T}(s_0,m_0)$ is the normal temperature in the month m_0 according to Equation 3, and $\delta T(s_0,d_0)$ is the daily temperature anomaly at the interpolation point s_0 for the day d_0.

Unlike traditional CAI applications, we employed spatial predictors in $\overline{T}(s_0,m_0)$ and $\delta T(s_0,d_0)$[13,39]. Some research have found that topographic factors in a mountainous region are directly related to the spatial patterns of $\delta T(s_0,d_0)$, particularly during stable atmospheric conditions that favour cold air inversion[13,93].

Data Records

The generated dataset consists of gridded, geo-localised files and a chart presenting information on the weather stations used. For quick access, the data are divided into different repositories and are stored in a figshare collection[113]: https://doi.org/10.6084/m9.figshare.c.5959863

- Repository 1: data of normal (average) and daily Tmax values. Files are all in Network Common Data Form (NetCDF) format.
- Repository 2: data of normal (average) and daily Tmin values. Files in NetCDF.
- Repository 3: data of spatial co-variables used. Files in NetCDF.
- Repository 4: list of weather stations used (Figure 2). File in Comma Separated Values (CSV).

It is crucial to mention that each NetCDF file contains three dimensions (*time*, *latitude*, and *longitude* represented by the date, latitude, and longitude, respectively). In the files with monthly normals (Tmax, Tmin, LST_day, and LST_night) the *time* dimension is *month*, which refers to the numeric value of a month of the year (beginning from January). For further information on each repository, see Supplementary Table 1.

Technical Validation

The development process of PISCOt has been evaluated in four steps: i) gap-filling validation; (ii) monthly normal validation; (iii) daily temperature validation; and (iv) comparison with other datasets of air temperature.

The statistics used to evaluate the skill of each step were simple error (mean bias), mean absolute error (MAE), and the refined index of agreement (d_r)[114]. The d_r metric ranges from -1.0 to 1.0, with a value of > 0.5 indicating a higher predictive capacity than the observed average. Because the primary mode of variability in temperature is usually the seasonal cycle, the metrics were calculated independently for each month and then averaged. This baseline adjustment in d_r prevented from overestimating the skill of each reconstruction (i.e. gap-filling, etc.) by correcting for the seasonal cycle[115].

Gap-filling validation

A gap-filling procedure was applied to extend shorter weather stations (back to 1981) before the construction of PISCOt. Two analysis were conducted to evaluate the efficiency of the gap-filling procedure: (i) validation using available data (comparing the gap-filled data with available observed data); and (ii) cross-validation, assuming that there are only ten years of data in those stations with more observed data (in time series with $\geq 75\%$ of non-missing data in the period 1981-2020).

Table 1 summarises the statistical metrics, and Figure 3 shows the distribution of d_r for both experiments. The experiments showed that the efficiency was slightly better for Tmax than Tmin. Both experiments had a bias < 0.2 C° and MAE < 1.5 C°. The most significant difference was in d_r; although moderate-to-high efficiency values were obtained in both experiments ($d_r > 0.5$), the best results were obtained in experiment (i). This can be explained due to the small amount of information available in the experiment (ii), as it was a worst-case scenario. By visualising the spatial distribution of d_r, it was noted that there were higher (lower) values in more (less) dense regions of weather stations for both experiments. The areas where d_r reached values from 0.8 to 0.9 were found in experiment (i). On the other hand, in experiment (ii), it reached values from 0.6 to 0.7.

In general, the validation errors showed that the here-in used infill models worked reasonably well, considering the complicated topographic variability of the study area and the limited observational data. It must be pointed out that the errors of experiment (i) represented the residuals between the filled and observed values, as these were used to construct the infilled models that were finally used in PISCOt.

Monthly normal validation

K-fold cross-validation was performed to characterise the efficiency of the spatial model for the monthly normal temperature. In this study, K = 10 was defined. Therefore, 10 clusters were set up for each model and data series. We applied the statistical metrics (bias and MAE) at the scale of two seasonal periods: "warm" (October to March) and "cold" (April to September).

Figure 4 showed a smaller positive bias in Tmax than in Tmin, with an average (warm and cold) value of 0.15 °C and 0.25 °C, respectively. However, this may be biased due to negative errors in the average. Considering the biases at the station scale, more points fall within the range of -1 °C to 1 °C in Tmin, implying that the estimation was better for Tmin. This pattern confirmed the findings for MAE, where Tmin (Tmax) averages 1.22 °C (1.4 °C) for both seasons. Spatially, the monthly normal interpolation performed worst in the mountainous regions between the boundaries of the climatic regions (Pacific Coast - Andes and Andes - Amazon), mainly in Tmax. Similarly, the largest errors in Tmax can be found in the southern Pacific Coast. At the seasonal level, there was no considerable difference in Tmax. However, for Tmin, estimates were slightly better in the warm period than in the cold period.

These results showed that the monthly normal interpolation for Tmin tends to be more efficient than for Tmax. In order to understand the impact of the spatial predictors (LST and DEM) on the air temperature estimation, the Lindemann, Merenda, and Gold (LMG) method was applied[13,116,117]. This method quantifies the relative influence of a spatial covariate by partitioning the total variance explained by the R^2 of the model. Figure 5 shows the results of this analysis.

In Tmax (Figure 5a), the DEM had the highest relative importance. The DEM contributed more in summer than in winter months, reaching values of up to 50% (40%) of the explained variance. LST, on the other hand, mainly relevant from summer to autumn. One probable reason why DEM was such a good predictor for Tmax is that Tmax generally has a simple linear decreasing relationship with DEM, and DEM already has a solid predictive capacity without the addition of LST[13,28,118]. In addition, due to the influence of solar radiation on the thermal infrared signal, different land cover mediating effects, moisture regimes on the surface energy balance, and higher daytime convective turbulence and advection compared to night-time conditions, the relationship between Tmax and LST is often more complex than that between Tmin and LST[13].

For Tmin, LST was a slightly more critical predictor than DEM in most months except for February (Figure 5b). However, no covariate reached a relative importance of 50%. It is somewhat noticeable that LST reached its highest values from June to November and, inversely, in DEM. Due to the strong gradients and complex topography, micro-climatic influences on Tmin play an essential role. Cold air inversions are a common phenomenon, especially during periods of atmospheric stability and significant radiative cooling which is typical for mountainous regions[28,93]. Therefore, Tmin does not have a simple linear relationship with DEM, which can limit its capacity as an individual predictor for the spatial patterns of Tmin[119]. The addition of LST, however, contributed to the spatial estimation of Tmin. This is also shown by the fact that higher values of R^2 were reached with Tmin (Figure 5c) than with Tmax.

In summary, it was shown that the spatial model used had a greater predictive capacity and a lower average error in the estimation of Tmin than Tmax, mainly during the summer months. LST had a higher value-added in Tmin than in Tmax in the study region.Furthermore, DEM was more important for Tmax prediction.

Daily temperature validation

The evaluation of the efficiency of daily air temperature data was similar to the one presented for the monthly normals, but only focused on the stations with long time series (with $\geq 75\%$ of non-missing data) to reduce the influence of synthetic data.

Figure 6 shows the results for bias and MAE, while Figure 7 shows the results for d_r. On average, a lower bias was observed compared to the normal scale. This was probably due to the greater amount of averaged data. Despite this, it can be observed that there was a similar pattern to the normal scale. In the bias (MAE), values of -0.01 °C and 0.05 °C (1.36 °C and 1.11 °C) were found on average at Tmax and Tmin, respectively. Furthermore, estimates were slightly better for Tmax (Tmin) in the cold (warm) period. d_r, reached moderate-to-high efficiency values ($d_r > 0.5$) at most of the weather stations. Efficiency values were lowest in the warm period of Tmax (d_r = 0.48). The area with the lowest d_r values was in the south, mainly along the Pacific Coast and the border regions of the Andes and the Amazon.

In general, the results demonstrated a reasonably good capacity of the spatial model to estimate daily Tmax and Tmin. Similarly, to the results from the normal monthly scale, Tmin outperformed Tmax in both the warm and cold periods.

Comparison of PISCOt with other datasets

To present an application of PISCOt v1.2, a description of the spatio-temporal variability of air temperature indices characterising the trend (the non-parametric Mann-Kendall test and Sen's slope estimator) was conducted. This was applied in the southern Andes of Peru, a region characterised by agricultural and livestock subsistence and production[42], and therefore highly dependent on climatic conditions. The indices selected were annual mean Tmax (MTmax), annual mean Tmin (MTmin), and the annual number of frost days (FD, number of days with Tmin < 0 °C).

Additionally, for comparison purposes, different gridded air-temperature products were used. In addition to the national products mentioned above (PISCOt v1.1 and VS2018), global products such as TerraClimate[120], CHIRTS[9], and ERA5-Land[76] were also used. TerraClimate provides Tmax and Tmin at monthly temporal resolution and a ∼4 km spatial resolution for 1958–2020. CHIRTS produces daily values of Tmax and Tmin at 5 km (0.05°) and is available from 1983 to 2016. ERA5-Land is a reanalysis product that contains a great diversity of surface variables at a spatial resolution of 9 km (∼0.1°) since 1981. For ERA5-Land, daily Tmax and Tmin were obtained from the maximum and minimum hourly values.

First, the spatial differences for the annual average air temperature indices were examined for the period 1981–2010. Figure 8a shows the annual climatologies of MTmax, MTmin, and FD in PISCOt v1.2, while Figure 8b indicates the difference of PISCOt v1.2 with each gridded product. For MTmax, differences were small (below 1 °C), mainly in PISCOt v1.1 and VS2018. ERA5-Land presented the lowest MTmax values compared to PISCOt v1.2, reaching differences of up to more than 6 °C in large parts of the Andean and Amazonian regions. The largest areas of differences between the multiple gridded products occured at the boundaries of the climatic regions, i.e., at the Andes-Amazon and Pacific-Andean transitions and where no data were available. For MTmin, the spatial pattern of the differences was similar to MTmax for PISCOt v1.1 and VS2018. The largest differences were found in TerraClimate and CHIRTS, where the latter had the highest MTmin values, reaching differences of up to more than -6 °C in the Andean highlands. For FD, PISCOt v1.1 and ERA5-Land showed the best agreement with PISCO v1.2 (differences within 10%). Only in CHIRTS differences of up to 60% were discovered. This was not surprising as CHIRTS was the most diverging product regarding Tmin.

The spatio-temporal variability of air temperature indices was assessed through trend analysis at different temporal and spatial windows. Figure 9 shows the decadal rate of change for 10-year time windows from 1981 to 2020 for areas above 2000 masl in the Southern Andes of Peru. For MTmax, there was a good agreement between the trends of the different products. Periods with significant positive trend were coinciding well in all products in the 1990–1995, 2000–2005, and 2010–2015 years. Periods with slightly negative or zero trends coinciding well in all products in the 1995–2000 and 2005–2010 years. This was evident in PISCOt v1.2 compared to ERA5-Land, VS2018, and PISCOt v1.1. For MTmin, there was more variability in the trends, with no clear overall direction as in MTmax, except for the latest years (since 2010). From 1980 to 2000, PISCOt v1.2 showed similar variability (a slightly positive trend) to ERA5-Land, then moves closer (a slightly negative trend) to PISCOt v1.1 and VS2018 in the 2000-2007 period, and finally, since 2010, being in agreement with PISCOt v1.1 and VS2018 and ERA5-Land into a positive trend. It is worth noting that PISCOt v1.1 and VS2018 showed good agreement in Tmin throughout the analysis period, diverging to a greater extent from PISCOt v1.2 before 1990. Significant positive trends in common in MTmin were only found during 1990-1995 and 2010-2015. A similar pattern as for MTmin was also found for FD. ERA5-Land (PISCOt v1.1) tended to behave analogously to PISCOt v1.2 for much of the analysis period, only disagreement (agreement) from 1995 to 2007. There were only significant overlapping trends in FD during 1990–1995 (negative) and 2010–2015 (positive).

Regarding spatial variability, Figure 10 shows the trend by different elevation intervals for the period 1983–2013 (common reporting period). In MTmax, the magnitude of trends increased for higher elevation intervals mainly in PISCOt v1.2, PISCOt v1.1, VS2018, and ERA5-Land. In contrast, in CHIRTS (TerraClimate) no relationship between the elevation and trend magnitude was evident. There was a more substantial spatial disparity in the direction of the trends at lower than high elevations in the different products (Supplementary Fig. 5). For Mtmin, the various products (except for CHIRTS) showed a better agreement of the relationship between the trend magnitude and elevation. However, this was less pronounced than for MTmax. Significant positive or negative trends in FD were only found between 3000 and 3500 masl, with a similar (inverse) agreement of PISCOt v1.2 with PISCOt v1.1 and ERA5-Land (CHIRTS). PISCOt v1.2 and ERA5-Land reached zero trends above 5000 masl, because for this elevation level for every year 100% FD was reached. Consequently, no temporal change can be found.

The results showed that PISCOt v1.2 performed well over the southern Andes of Peru. PISCOt v1.2 presented spatiotemporal trends and overall distribution similar to the other products. Some differences in the results can be pointed out. Firstly, there was a high degree of correspondance in the magnitude of the air temperature between PISCOt v1.2 and PISCOt v1.1 and VS2018. This was expected, since the three datasets used information from the same station's network, albeit with a different number of stations and distinct pre-processing applied. Larger differences were obtained in ERA5-Land (MTmax) and CHIRTS (in MTmin and FD). ERA5-Land is a reanalysis-based dataset, thus, it is expected to represent the physics. However, it was subject to systematic differences caused by the misrepresentation of the topography, requiring a bias correction prior to its use at high elevations[121]. CHIRTS was a mixture of station-based and reanalysis data. In its construction, it prioritised the estimation of Tmax rather than Tmin[9], possibly explaining the significant differences with the latter variable. Considering the trends, there was a clear warming signal[5,38], with larger magnitudes and spatially more homogeneous in Tmax than in Tmin[42]. CHIRTS and TerraClimate disagreed the most in temporal and spatial trends, leading to large unphysical trends due to unhomogenized or missing station data. This is an issue that should be fixed by using homogenisation algorithms.

Usage Notes

The PISCOt v1.2 database is a valuable dataset for different applications as it allows for the first time local and regional applications in Peru at grid level for studies linked to climate change, health, hydrology, ecosystem assessments, and other fields for research and practitioners. It supports the generation of new findings urgently required for more robust local decision-making in the scientific and political communities, especially in a context of data scarcity and high uncertainties in the region.

The new PISCOt v1.2 product has improved compared to the earlier version 1.1 in several key aspects: more assimilated time series, better consistency of station data pre-processing (quality control, gap-filling, and homogenisation), use of updated freely available auxiliary predictors, higher spatial resolution, a tidier and revised calculation sequence, and improved version control. Therefore, the development of PISCOt v1.2 is more consistent, traceable, and reproducible compared to other previously established gridded products in Peru.

PISCOt v1.2 adequately characterises the spatiotemporal variability of air temperature in average and extreme values using indicators. However, within the scope of this study only three indices were used. Future assessments therefore need to focus on more indicators of climate extremes not assessed in this study.

As the region is topographically complex, including steep climatic gradients, has a low density and uneven distribution of weather stations, inherent limitations in spatial interpolation are expected, mainly at high elevations (between 1000 and 2000 masl, and $>$ 3500 masl). It is thus recommended to use PISCOt v1.2 along with other gridded multi-source products which would allow for a better characterisation of the associated uncertainties in air temperature.

Further, it is essential to clarify that matching weather stations with PISCOt v1.2 (and other products) is not recommended for assessing air temperature accuracy[122]. This is because such an analysis would favour products with interpolation algorithms that constrain the gridded data to precisely match weather station data. Likewise, if processes such as gap-filling, and homogeneity correction, among others, are applied to the observed data before spatial interpolation, the updated information would therefore no longer match the original data.

Finally, the gridded data of PISCOt v1.2 should only be used for continental areas. Due to the differences in LST values over water bodies compared to their surrounding terrestrial landscapes and the lack of observations over lakes, further validation is required to confirm the accuracy of air temperature spatial patterns over the water[13]. Estimates over e.g. water bodies should be masked (i.e. be considered as empty grids).

Code availability

Construction of the gridded data was performed using the R (v3.6.3) and Python (v3.8.5) programming languages. The entire code used to construct PISCOt is freely available at figshare and GitHub (https://github.com/adrHuerta/PISCOt_v1-2) under GNU public license version 3.

References

1. Kessler, M., Toivonen, J. M., Sylvester, S. P., Kluge, J. & Hertel, D. Elevational patterns of polylepis tree height (rosaceae) in the high andes of peru: role of human impact and climatic conditions. *Front. plant science* **5**, 194, https://doi.org/10.3389/fpls.2014.00194 (2014).

2. Rau, P. *et al.* Assessing multidecadal runoff (1970–2010) using regional hydrological modelling under data and water scarcity conditions in peruvian pacific catchments. *Hydrol. Process.* **33**, 20–35, https://doi.org/10.1002/hyp.13318 (2019).

3. Delahoy, M. J. *et al.* Meteorological factors and childhood diarrhea in peru, 2005–2015: a time series analysis of historic associations, with implications for climate change. *Environ. Heal.* **20**, 1–10, https://doi.org/10.1186/s12940-021-00703-4 (2021).

4. Sanabria, J., Calanca, P., Alarcón, C. & Canchari, G. Potential impacts of early twenty-first century changes in temperature and precipitation on rainfed annual crops in the Central Andes of Peru. *Reg. Environ. Chang.* **14**, 1533–1548, https://doi.org/10.1007/s10113-014-0595-y (2014).

5. López-Moreno, J. I. *et al.* Recent temperature variability and change in the Altiplano of Bolivia and Peru. *Int. J. Climatol.* **36**, 1773–1796, https://doi.org/10.1002/joc.4459 (2016).

6. Sulca, J. *et al.* Climatology of extreme cold events in the central Peruvian Andes during austral summer: origin, types and teleconnections. *Q. J. Royal Meteorol. Soc.* https://doi.org/10.1002/qj.3398 (2018).

7. Harris, I., Osborn, T. J., Jones, P. & Lister, D. Version 4 of the cru ts monthly high-resolution gridded multivariate climate dataset. *Sci. data* **7**, 1–18, https://doi.org/10.1038/s41597-020-0453-3 (2020).

8. Hersbach, H. *et al.* The era5 global reanalysis. *Q. J. Royal Meteorol. Soc.* **146**, 1999–2049, https://doi.org/10.1002/qj.3803 (2020).

9. Verdin, A. *et al.* Development and validation of the chirts-daily quasi-global high-resolution daily temperature data set. *Sci. Data* **7**, 1–14, https://doi.org/10.1038/s41597-020-00643-7 (2020).

10. Dee, D. P. *et al.* The era-interim reanalysis: Configuration and performance of the data assimilation system. *Q. J. Royal Meteorol. Soc.* **137**, 553–597, 10.1002/qj.828 (2011).

11. Rao, Y., Liang, S. & Yu, Y. Land Surface Air Temperature Data Are Considerably Different Among BEST-LAND, CRU-TEM4v, NASA-GISS, and NOAA-NCEI. *J. Geophys. Res. Atmospheres* **123**, 5881–5900, https://doi.org/10.1029/2018JD028355 (2018).

12. Krähenmann, S. & Ahrens, B. Spatial gridding of daily maximum and minimum 2 m temperatures supported by satellite observations. *Meteorol. Atmospheric Phys.* **120**, 87–105, https://doi.org/10.1007/s00703-013-0237-9 (2013).

13. Oyler, J. W., Ballantyne, A., Jencso, K., Sweet, M. & Running, S. W. Creating a topoclimatic daily air temperature dataset for the conterminous United States using homogenized station data and remotely sensed land skin temperature. *Int. J. Climatol.* **35**, 2258–2279, https://doi.org/10.1002/joc.4127 (2015).

14. Hiebl, J. & Frei, C. Daily temperature grids for Austria since 1961—concept, creation and applicability. *Theor. Appl. Climatol.* **124**, 161–178, https://doi.org/10.1007/s00704-015-1411-4 (2016).

15. Berezowski, T. *et al.* CPLFD-GDPT5: High-resolution gridded daily precipitation and temperature data set for two largest Polish river basins. *Earth Syst. Sci. Data* **8**, 127–139, https://doi.org/10.5194/essd-8-127-2016 (2016).

16. Antolini, G. *et al.* A daily high-resolution gridded climatic data set for Emilia-Romagna, Italy, during 1961-2010. *Int. J. Climatol.* **36**, 1970–1986, https://doi.org/10.1002/joc.4473 (2016).

17. Way, R. G., Lewkowicz, A. G. & Bonnaventure, P. P. Development of moderate-resolution gridded monthly air temperature and degree-day maps for the Labrador-Ungava region of northern Canada. *Int. J. Climatol.* **37**, 493–508, https://doi.org/10.1002/joc.4721 (2017).

18. Fonseca, A. R. & Santos, J. A. High-resolution temperature datasets in Portugal from a geostatistical approach: Variability and extremes. *J. Appl. Meteorol. Climatol.* **57**, 627–644, https://doi.org/10.1175/JAMC-D-17-0215.1 (2018).

19. Li, J. & Heap, A. D. A review of comparative studies of spatial interpolation methods in environmental sciences: Performance and impact factors. *Ecol. Informatics* **6**, 228–241, 10.1016/j.ecoinf.2010.12.003 (2011). 1010.1236.

20. Li, J. & Heap, A. D. Spatial interpolation methods applied in the environmental sciences: A review. *Environ. Model. Softw.* **53**, 173–189, 10.1016/j.envsoft.2013.12.008 (2014).

21. Shen, H. *et al.* Deep learning-based air temperature mapping by fusing remote sensing, station, simulation and socioeconomic data. *Remote. Sens. Environ.* **240**, 111692 (2020).

22. Zhang, X. *et al.* Deep learning-based 500 m spatio-temporally continuous air temperature generation by fusing multi-source data. *Remote. Sens.* **14**, 3536 (2022).

23. Sekulić, A., Kilibarda, M., Protić, D. & Bajat, B. A high-resolution daily gridded meteorological dataset for serbia made by random forest spatial interpolation. *Sci. Data* **8**, 1–12 (2021).

24. He, Q., Wang, M., Liu, K., Li, K. & Jiang, Z. Gprchinatemp1km: a high-resolution monthly air temperature data set for china (1951–2020) based on machine learning. *Earth Syst. Sci. Data* **14**, 3273–3292 (2022).

25. Lary, D. J., Alavi, A. H., Gandomi, A. H. & Walker, A. L. Machine learning in geosciences and remote sensing. *Geosci. Front.* **7**, 3–10, https://doi.org/10.1016/j.gsf.2015.07.003 (2016).

26. Hengl, T., Nussbaum, M., Wright, M. N., Heuvelink, G. B. & Gräler, B. Random forest as a generic framework for predictive modeling of spatial and spatio-temporal variables. *PeerJ* **6**, e5518 (2018).

27. Hernanz, A., García-Valero, J. A., Domínguez, M. & Rodríguez-Camino, E. A critical view on the suitability of machine learning techniques to downscale climate change projections: Illustration for temperature with a toy experiment. *Atmospheric Sci. Lett.* e1087 (2022).

28. Daly, C. *et al.* Physiographically sensitive mapping of climatological temperature and precipitation across the conterminous United States. *Int. J. Climatol.* **28**, 2031–2064, 10.1002/joc.1688 (2008). joc.1492.

29. Hengl, T., Heuvelink, G. B., Tadić, M. P. & Pebesma, E. J. Spatio-temporal prediction of daily temperatures using time-series of MODIS LST images. *Theor. Appl. Climatol.* **107**, 265–277, 10.1007/s00704-011-0464-2 (2012).

30. Lin, G. *et al.* Spatio-temporal variation of PM2.5concentrations and their relationship with geographic and socioeconomic factors in China. *Int. J. Environ. Res. Public Heal.* **11**, 173–186, 10.3390/ijerph110100173 (2013).

31. Kilibarda, M. *et al.* Spatio-temporal interpolation of daily temperatures for global land areas at 1 km resolution. *J. Geophys. Res.* **119**, 2294–2313, 10.1002/2013JD020803 (2014).

32. Wang, M. *et al.* Comparison of spatial interpolation and regression analysis models for an estimation of monthly near surface air temperature in China. *Remote. Sens.* **9**, 10.3390/rs9121278 (2017).

33. Xavier, A. C., King, C. W. & Scanlon, B. R. Daily gridded meteorological variables in Brazil (1980–2013). *Int. J. Climatol.* **36**, 2644–2659, https://doi.org/10.1002/joc.4518 (2016). 1311.1716.

34. Xavier, A. C., Scanlon, B. R., King, C. W. & Alves, A. I. New improved brazilian daily weather gridded data (1961-2020). *Int. J. Climatol.* (2022).

35. Bianchi, E., Villalba, R., Viale, M., Couvreux, F. & Marticorena, R. New precipitation and temperature grids for northern Patagonia: Advances in relation to global climate grids. *J. Meteorol. Res.* **30**, 38–52, https://doi.org/10.1007/s13351-015-5058-y (2016).

36. Vicente-Serrano, S. M. *et al.* Average monthly and annual climate maps for Bolivia. *J. Maps* **12**, 295–310, https://doi.org/10.1080/17445647.2015.1014940 (2016).

37. Andrade, M. F. *et al.* Atlas-clima y eventos extremos del altiplano central perú-boliviano. *Geogr. Bernensia* https://doi.org/10.4480/GB2018.N01 (2018).

38. Vicente-Serrano, S. M. *et al.* Recent changes in monthly surface air temperature over Peru, 1964–2014. *Int. J. Climatol.* **38**, 283–306, https://doi.org/10.1002/joc.5176 (2018).

39. Huerta, A., Aybar, C. & Lavado-Casimiro, W. PISCO temperatura versión 1.1 (PISCOt v1. 1). *Lima, Peru: Natl. Meteorol. Hydrol. Serv. Peru (SENAMHI)* https://iridl.ldeo.columbia.edu/SOURCES/.SENAMHI/.HSR/.PISCO/.Temp/ (2018).

40. Drenkhan, F., Huggel, C., Guardamino, L. & Haeberli, W. Managing risks and future options from new lakes in the deglaciating andes of peru: The example of the vilcanota-urubamba basin. *Sci. Total. Environ.* **665**, 465–483 (2019).

41. Muñoz, R., Huggel, C., Drenkhan, F., Vis, M. & Viviroli, D. Comparing model complexity for glacio-hydrological simulation in the data-scarce peruvian andes. *J. Hydrol. Reg. Stud.* **37**, 100932 (2021).

42. Imfeld, N. *et al.* A combined view on precipitation and temperature climatology and trends in the southern andes of peru. *Int. journal climatology* **41**, 679–698, https://doi.org/10.1002/joc.6645 (2021).

43. Llauca, H., Lavado-Casimiro, W., Montesinos, C., Santini, W. & Rau, P. Pisco_hym_gr2m: A model of monthly water balance in peru (1981–2020). *Water* **13**, 1048, https://doi.org/10.3390/w13081048 (2021).

44. Monge-Salazar, M. J. *et al.* Ecohydrology and ecosystem services of a natural and an artificial bofedal wetland in the central andes. *Sci. The Total. Environ.* 155968 (2022).

45. Motschmann, A. *et al.* Current and future water balance for coupled human-natural systems–insights from a glacierized catchment in peru. *J. Hydrol. Reg. Stud.* **41**, 101063 (2022).

46. Chen, F., Liu, Y., Liu, Q. & Qin, F. A statistical method based on remote sensing for the estimation of air temperature in China. *Int. J. Climatol.* **35**, 2131–2143, 10.1002/joc.4113 (2015).

47. Oyler, J. W., Dobrowski, S. Z., Holden, Z. A. & Running, S. W. Remotely sensed land skin temperature as a spatial predictor of air temperature across the conterminous United States. *J. Appl. Meteorol. Climatol.* **55**, 1441–1457, 10.1175/JAMC-D-15-0276.1 (2016).

48. Kloog, I. *et al.* Modelling spatio-temporally resolved air temperature across the complex geo-climate area of France using satellite-derived land surface temperature data. *Int. J. Climatol.* **37**, 296–304, 10.1002/joc.4705 (2017).

49. Li, X., Zhou, Y., Asrar, G. R. & Zhu, Z. Developing a 1 km resolution daily air temperature dataset for urban and surrounding areas in the conterminous United States. *Remote. Sens. Environ.* **215**, 74–84, 10.1016/j.rse.2018.05.034 (2018).

50. Woldesenbet, T. A., Elagib, N. A., Ribbe, L. & Heinrich, J. Gap filling and homogenization of climatological datasets in the headwater region of the Upper Blue Nile Basin, Ethiopia. *Int. J. Climatol.* **37**, 2122–2140, https://doi.org/10.1002/joc.4839 (2017).

51. Hunziker, S. *et al.* Identifying, attributing, and overcoming common data quality issues of manned station observations. *Int. J. Climatol.* **37**, 4131–4145, https://doi.org/10.1002/joc.5037 (2017).

52. Huerta, A. & Lavado-Casimiro, W. *Atlas de Zonas Áridas del Perú: una evaluación presente y futura* (Servicio Nacional de Meteorología e Hidrología del Perú, Lima, Perú, 2021).

53. Zevallos, J. & Lavado-Casimiro, W. Climate change impact on peruvian biomes. *Forests* **13**, 238 (2022).

54. Dawdy, D. & Langbein, W. Mapping mean areal precipitation. *Hydrol. Sci. J.* **5**, 16–23 (1960).

55. Willmott, C. J. & Robeson, S. M. Climatologically aided interpolation (CAI) of terrestrial air temperature. *Int. J. Climatol.* **15**, 221–229, 10.1002/joc.3370150207 (1995).

56. New, M., Hulme, M. & Jones, P. Representing twentieth-century space–time climate variability. part ii: Development of 1901–96 monthly grids of terrestrial surface climate. *J. climate* **13**, 2217–2238, https://doi.org/10.1175/1520-0442(2000)013<2217:RTCSTC>2.0.CO;2 (2000).

57. Hunter, R. D. & Meentemeyer, R. K. Climatologically aided mapping of daily precipitation and temperature. *J. Appl. Meteorol.* **44**, 1501–1510, https://doi.org/10.1175/JAM2295.1 (2005).

58. Condom, T. *et al.* Climatological and hydrological observations for the south american andes: in situ stations, satellite, and reanalysis data sets. *Front. Earth Sci.* **8**, 92 (2020).

59. Hubbard, K. Spatial variability of daily weather variables in the high plains of the usa. *Agric. For. Meteorol.* **68**, 29–41, https://doi.org/10.1016/0168-1923(94)90067-1 (1994).

60. Camargo, M. B. & Hubbard, K. G. Spatial and temporal variability of daily weather variables in sub-humid and semi-arid areas of the united states high plains. *Agric. forest meteorology* **93**, 141–148, https://doi.org/10.1016/S0168-1923(98)00122-1 (1999).

61. Vera, L., Villegas, E., Oria, C. & Arboleda, F. Control de calidad de datos de estaciones meteorológicas e hidrológicas automáticas en el centro de procesamiento de datos del senamhi. Tech. Rep., Servicio Nacional de Meteorología e Hidrología del Perú (SENAMHI) (2021). https://www.senamhi.gob.pe/load/file/00711SENA-54.pdf.

62. Espinoza, J. C. *et al.* Revisiting wintertime cold air intrusions at the east of the andes: propagating features from subtropical argentina to peruvian amazon and relationship with large-scale circulation patterns. *Clim. dynamics* **41**, 1983–2002 (2013).

63. Vicente-Serrano, S. M., Beguería, S., López-Moreno, J. I., García-Vera, M. A. & Stepanek, P. A complete daily precipitation database for northeast spain: reconstruction, quality control, and homogeneity. *Int. J. Climatol.* **30**, 1146–1163, https://doi.org/10.1002/joc.1850 (2010).

64. Tomas-Burguera, M., Vicente-Serrano, S. M., Beguería, S., Reig, F. & Latorre, B. Reference crop evapotranspiration database in spain (1961–2014). *Earth Syst. Sci. Data* **11**, 1917–1930, https://doi.org/10.5194/essd-11-1917-2019 (2019).

65. Huerta, A. & Lavado-Casimiro, W. Trends and variability of precipitation extremes in the peruvian altiplano (1971–2013). *Int. J. Climatol.* **41**, 513–528 (2021).

66. Huerta, A. *et al.* Piscoeo_pm, a reference evapotranspiration gridded database based on fao penman-monteith in peru. *Sci. data* **9**, 1–18, https://doi.org/10.1038/s41597-022-01373-8 (2022).

67. Hunziker, S. *et al.* Effects of undetected data quality issues on climatological analyses. *Clim. Past* **14**, 1–20, https://doi.org/10.5194/cp-14-1-2018 (2018).

68. Guentchev, G., Barsugli, J. J. & Eischeid, J. Homogeneity of gridded precipitation datasets for the colorado river basin. *J. Appl. Meteorol. Climatol.* **49**, 2404–2415, https://doi.org/10.1175/2010JAMC2484.1 (2010).

69. Aybar, C. *et al.* Construction of a high-resolution gridded rainfall dataset for peru from 1981 to the present day. *Hydrol. Sci. J.* **65**, 770–785, https://doi.org/10.1175/2010JAMC2484.1 (2020).

70. Beguería, S., Vicente-Serrano, S. M., Tomás-Burguera, M. & Maneta, M. Bias in the variance of gridded data sets leads to misleading conclusions about changes in climate variability. *Int. J. Climatol.* **36**, 3413–3422, https://doi.org/10.1002/joc.4561 (2016).

71. Thevakaran, A. & Sonnadara, D. U. Estimating missing daily temperature extremes in Jaffna, Sri Lanka. *Theor. Appl. Climatol.* **132**, 145–152, https://doi.org/10.1007/s00704-017-2082-0 (2018).

72. Beguería, S. *et al.* Gap filling of monthly temperature data and its effect on climatic variability and trends. *J. Clim.* **32**, 7797–7821, https://doi.org/10.1175/JCLI-D-19-0244.1 (2019).

73. Gudmundsson, L., Bremnes, J. B., Haugen, J. E. & Engen-Skaugen, T. Downscaling rcm precipitation to the station scale using statistical transformations–a comparison of methods. *Hydrol. Earth Syst. Sci.* **16**, 3383–3390, https://doi.org/10.5194/hess-16-3383-2012 (2012).

74. Stanley, T., Kirschbaum, D. B., Huffman, G. J. & Adler, R. F. Approximating long-term statistics early in the global precipitation measurement era. *Earth Interactions* **21**, 1–10, https://doi.org/10.1175/EI-D-16-0025.1 (2017).

75. Gonzalez-Hidalgo, J. C., Peña-Angulo, D., Brunetti, M. & Cortesi, N. Motedas: a new monthly temperature database for mainland spain and the trend in temperature (1951–2010). *Int. J. Climatol.* **35**, 4444–4463, https://doi.org/10.1002/joc.4298 (2015).

76. Muñoz-Sabater, J. *et al.* Era5-land: A state-of-the-art global reanalysis dataset for land applications. *Earth Syst. Sci. Data Discuss.* 1–50, https://doi.org/10.5194/essd-13-4349-2021 (2021).

77. Cannon, A. J., Sobie, S. R. & Murdock, T. Q. Bias correction of gcm precipitation by quantile mapping: How well do methods preserve changes in quantiles and extremes? *J. Clim.* **28**, 6938–6959, https://doi.org/10.1175/JCLI-D-14-00754.1 (2015).

78. Venema, V. K. C. *et al.* Benchmarking homogenization algorithms for monthly data. *Clim. Past* **8**, 89–115, https://doi.org/10.5194/cp-8-89-2012 (2012).

79. Brönnimann, S. Climatic changes since 1700. In *Climatic Changes Since 1700*, 167–321 (Springer, 2015).

80. Domonkos, P., Guijarro, J. A., Venema, V., Brunet, M. & Sigró, J. Efficiency of time series homogenization: Method comparison with 12 monthly temperature test datasets. *J. Clim.* **34**, 2877 – 2891, https://doi.org/10.1175/JCLI-D-20-0611.1 (01 Apr. 2021).

81. Gubler, S. *et al.* The influence of station density on climate data homogenization. *Int. J. Climatol.* **37**, 4670–4683, https://doi.org/10.1002/joc.5114 (2017).

82. Alexandersson, H. A homogeneity test applied to precipitation data. *J. Climatol.* **6**, 661–675, https://doi.org/10.1002/joc.3370060607 (1986).

83. Haimberger, L. Homogenization of radiosonde temperature time series using innovation statistics. *J. Clim.* **20**, 1377 – 1403, https://doi.org/10.1175/JCLI4050.1 (01 Apr. 2007).

84. Menne, M. J. & Williams, C. N. Homogenization of temperature series via pairwise comparisons. *J. Clim.* **22**, 1700–1717, https://doi.org/10.1175/2008JCLI2263.1 (2009).

85. Browning, J. & Schneider, C. *snht: Standard Normal Homogeneity Test* (2017). R package version 1.0.5.

86. Dunn, R. J. H., Willett, K. M., Morice, C. P. & Parker, D. E. Pairwise homogeneity assessment of hadisd. *Clim. Past* **10**, 1501–1522, https://doi.org/10.5194/cp-10-1501-2014 (2014).

87. Thorne, P. W. *et al.* Toward an integrated set of surface meteorological observations for climate science and applications. *Bull. Am. Meteorol. Soc.* **98**, 2689 – 2702, https://doi.org/10.1175/BAMS-D-16-0165.1 (01 Dec. 2017).

88. Brugnara, Y., Good, E., Squintu, A. A., van der Schrier, G. & Brönnimann, S. The eustace global land station daily air temperature dataset. *Geosci. Data J.* **6**, 189–204, https://doi.org/10.1002/gdj3.81 (2019).

89. Vincent, L. A., Zhang, X., Bonsal, B. R. & Hogg, W. D. Homogenization of daily temperatures over canada. *J. Clim.* **15**, 1322 – 1334, 10.1175/1520-0442(2002)015<1322:HODTOC>2.0.CO;2 (01 Jun. 2002).

90. Jin, M. & Dickinson, R. E. Land surface skin temperature climatology: Benefitting from the strengths of satellite observations. *Environ. Res. Lett.* **5**, 044004, https://doi.org/10.1088/1748-9326/5/4/044004 (2010).

91. Wan, Z., Hook, S. & Hulley, G. Modis/terra land surface temperature/emissivity 8-day l3 global 1km sin grid v006, https://doi.org/10.5067/MODIS/MOD11A2.006 (2015).

92. Danielson, J. J. & Gesch, D. B. *Global multi-resolution terrain elevation data 2010 (GMTED2010)* (US Department of the Interior, US Geological Survey, 2011).

93. Holden, Z. A., Abatzoglou, J. T., Luce, C. H. & Baggett, L. S. Empirical downscaling of daily minimum air temperature at very fine resolutions in complex terrain. *Agric. For. Meteorol.* **151**, 1066–1073, https://doi.org/10.1016/j.agrformet.2011.03.011 (2011).

94. Gorelick, N. *et al.* Google earth engine: Planetary-scale geospatial analysis for everyone. *Remote. sensing Environ.* **202**, 18–27, https://doi.org/10.1016/j.rse.2017.06.031 (2017).

95. Aybar, C., Wu, Q., Bautista, L., Yali, R. & Barja, A. rgee: An r package for interacting with google earth engine. *J. Open Source Softw.* **5**, 2272, https://doi.org/10.21105/joss.02272 (2020).

96. Parmentier, B. *et al.* Using multi-timescale methods and satellite-derived land surface temperature for the interpolation of daily maximum air temperature in Oregon. *Int. J. Climatol.* **35**, 3862–3878, https://doi.org/10.1002/joc.4251 (2015).

97. Longman, R. J. *et al.* High-resolution gridded daily rainfall and temperature for the hawaiian islands (1990–2014). *J. Hydrometeorol.* **20**, 489–508 (2019).

98. Newman, A. J. *et al.* Use of daily station observations to produce high-resolution gridded probabilistic precipitation and temperature time series for the hawaiian islands. *J. Hydrometeorol.* **20**, 509–529 (2019).

99. Newman, A. J., Clark, M. P., Wood, A. W. & Arnold, J. R. Probabilistic spatial meteorological estimates for alaska and the yukon. *J. Geophys. Res. Atmospheres* **125**, e2020JD032696 (2020).

100. Hengl, T., Heuvelink, G. & Rossiter, D. About regression-kriging: from theory to interpretation of results. *Comput. & Geosci.* **33**, 1301–1315, https://doi.org/10.1016/j.cageo.2007.05.001 (2007).

101. Hengl, T., Heuvelink, G. B., Tadić, M. P. & Pebesma, E. J. Spatio-temporal prediction of daily temperatures using time-series of modis lst images. *Theor. applied climatology* **107**, 265–277, https://doi.org/10.1007/s00704-011-0464-2 (2012).

102. Webster, R. & Oliver, M. A. *Geostatistics for environmental scientists* (John Wiley & Sons, 2007).

103. Harris, P., Fotheringham, A., Crespo, R. & Charlton, M. The use of geographically weighted regression for spatial prediction: an evaluation of models using simulated data sets. *Math. Geosci.* **42**, 657–680, https://doi.org/10.1007/s11004-010-9284-7 (2010).

104. Fotheringham, A. S., Brunsdon, C. & Charlton, M. *Geographically weighted regression: the analysis of spatially varying relationships* (John Wiley & Sons, 2003).

105. Gollini, I., Lu, B., Charlton, M., Brunsdon, C. & Harris, P. Gwmodel: An r package for exploring spatial heterogeneity using geographically weighted models. *J. Stat. Software, Articles* **63**, 1–50, https://doi.org/10.18637/jss.v063.i17 (2015).

106. Zhan, W. *et al.* Disaggregation of remotely sensed land surface temperature: Literature survey, taxonomy, issues, and caveats. *Remote. Sens. Environ.* **131**, 119–139, https://doi.org/10.1016/j.rse.2012.12.014 (2013).

107. Wang, S., Luo, X. & Peng, Y. Spatial downscaling of modis land surface temperature based on geographically weighted autoregressive model. *IEEE J. Sel. Top. Appl. Earth Obs. Remote. Sens.* **13**, 2532–2546, https://doi.org/10.1109/JSTARS.2020.2968809 (2020).

108. Zhang, X., Zwiers, F. W. & Hegerl, G. The influences of data precision on the calculation of temperature percentile indices. *Int. J. Climatol.* **29**, 321–327, https://doi.org/10.1002/joc.1738 (2009). https://rmets.onlinelibrary.wiley.com/doi/pdf/10.1002/joc.1738.

109. Rhines, A., Tingley, M. P., McKinnon, K. A. & Huybers, P. Decoding the precision of historical temperature observations. *Q. J. Royal Meteorol. Soc.* **141**, 2923–2933, https://doi.org/10.1002/qj.2612 (2015). https://rmets.onlinelibrary.wiley.com/doi/pdf/10.1002/qj.2612.

110. Pebesma, E. J. Multivariable geostatistics in s: the gstat package. *Comput. & geosciences* **30**, 683–691, https://doi.org/10.1016/j.cageo.2004.03.012 (2004).

111. Gräler, B., Pebesma, E. & Heuvelink, G. Spatio-Temporal Interpolation using gstat. *The R Journal* **8**, 204–218, https://doi.org/10.32614/RJ-2016-014 (2016).

112. Hiemstra, P., Pebesma, E., Twenhöfel, C. & Heuvelink, G. Real-time automatic interpolation of ambient gamma dose rates from the dutch radioactivity monitoring network. *Comput. Geosci.* http://dx.doi.org/10.1016/j.cageo.2008.10.011 (2008).

113. Huerta, A. PISCOt, a high-resolution gridded dataset of daily air temperature for Peru, https://doi.org/10.6084/m9.figshare.c.5959863 (2022).

114. Willmott, C. J., Robeson, S. M. & Matsuura, K. A refined index of model performance. *Int. J. Climatol.* **32**, 2088–2094, https://doi.org/10.1002/joc.2419 (2012).

115. Legates, D. R. & McCabe, G. J. A refined index of model performance: a rejoinder. *Int. J. Climatol.* **33**, 1053–1056, https://doi.org/10.1002/joc.3487 (2013).

116. Lindeman, R. H. Introduction to bivariate and multivariate analysis. Tech. Rep., Scott Foresman & Co (1980).

117. Grömping, U. Relative importance for linear regression in r: the package relaimpo. *J. statistical software* **17**, 1–27 (2007).

118. Dobrowski, S. Z., Abatzoglou, J. T., Greenberg, J. A. & Schladow, S. How much influence does landscape-scale physiography have on air temperature in a mountain environment? *Agric. For. Meteorol.* **149**, 1751–1758 (2009).

119. Moraes, A. G. d. L. *et al.* Terrain sensitive climate mapping for the arequipa department in peru. *Int. J. Climatol.* https://doi.org/10.1002/joc.7730 (2022).

120. Abatzoglou, J. T., Dobrowski, S. Z., Parks, S. A. & Hegewisch, K. C. TerraClimate, a high-resolution global dataset of monthly climate and climatic water balance from 1958-2015. *Sci. Data* **5**, 1–12, https://doi.org/10.1038/sdata.2017.191 (2018).

121. Bonshoms, M. *et al.* Validation of era5-land temperature and relative humidity on four peruvian glaciers using on-glacier observations. *J. Mountain Sci.* **19**, 1849–1873, https://doi.org/10.1007/s11629-022-7388-4 (2022).

122. Walton, D. & Hall, A. An assessment of high-resolution gridded temperature datasets over california. *J. Clim.* **31**, 3789–3810, https://doi.org/10.1175/JCLI-D-17-0410.1 (2018).

Acknowledgements

The new version of PISCOt was developed with support by the Newton-Paulet fund within the project 'Water security and climate change adaptation in Peruvian glacier-fed river basins' (RAHU) under the contract N°005-2019-FONDECYT. A.H. acknowledges additional financial support of the project "Natural Infrastructure for Water Security" (NIWS), an initiative promoted and financed by the United States Agency for International Development (USAID) and the Canadian Government. P.R. acknowledges support from the fund KF400238 British Academy: El Niño and flash floods in Peru: Bringing knowledge on "Furia de los rios" and "Western science" to understand lag time. We are grateful for the freely available global products: ERA5-Land climate reanalysis data from the Copernicus Climate Change Service (C3S) Climate Data Store at https://cds.climate.copernicus.eu/, the TerraClimate data from the Climatology Lab portal at https://www.climatologylab.org/terraclimate.html; and, the CHIRTS data from the Climatic Hazard Center at https://www.chc.ucsb.edu/data. In addition, PISCOt v1.1 was obtained from the IRI/LDEO Climate Data Library at http://iridl.ldeo.columbia.edu/SOURCES/.SENAMHI/.HSR/.PISCO/; and VS2018 from http://hdl.handle.net/10261/139347.

Author contributions statement

A.H. led the publication, wrote the first draft of the manuscript, and developed the methodology in consultation with W.L.C. A.H., C.A. and K.C. collected the station and satellite data. A.H. pre-processed the station data. A.H. and C.A produced the gridding of station data. A.H. and N.I. validated the data. O.F.B., P.R., F.D., and W.L.C. supervised the dataset construction and provided professional advice. All authors were involved in discussions with regard to data development, and all reviewed the manuscript.

Competing interests

The authors declare no competing interests.

799 # Figures & Tables

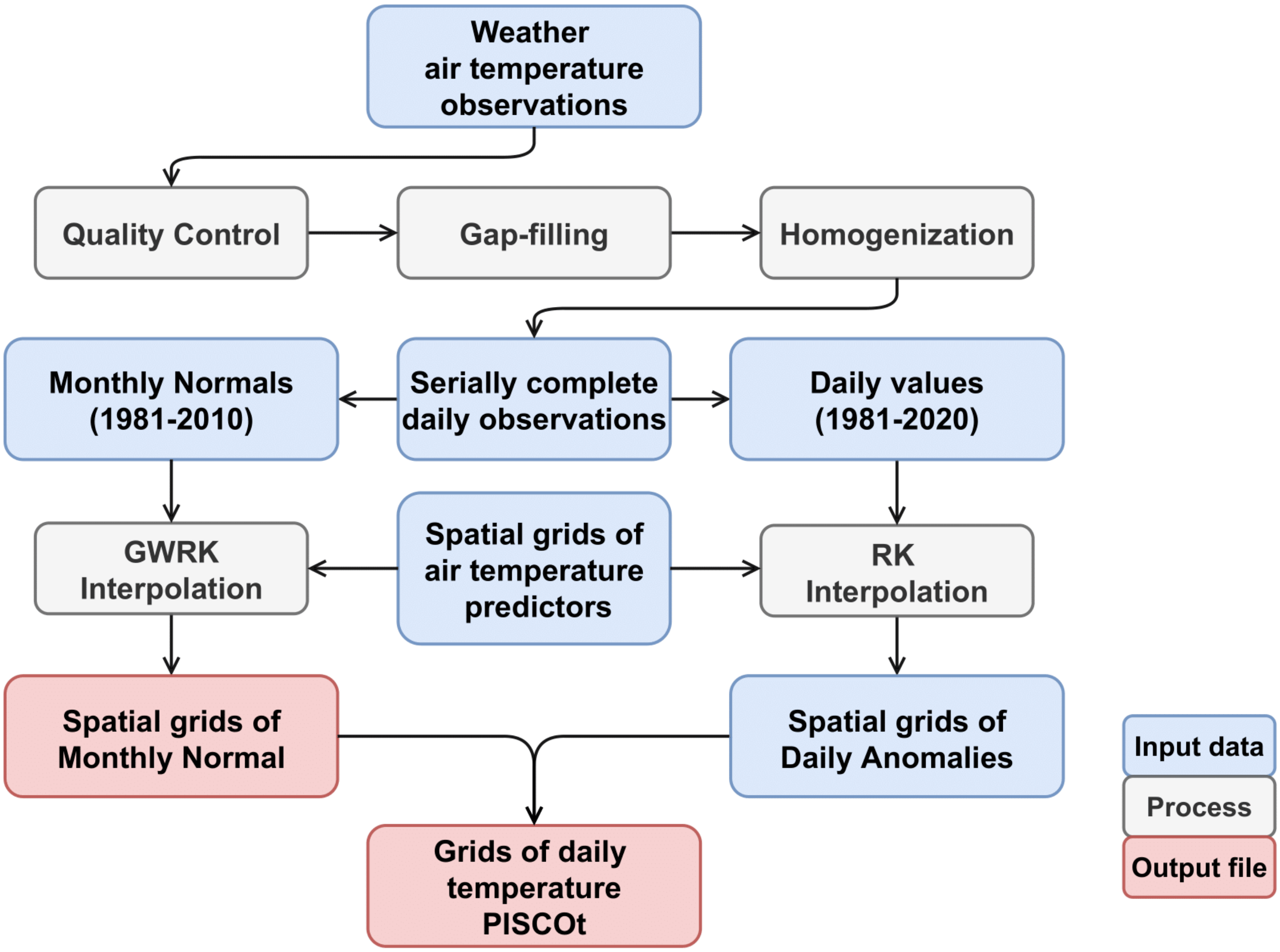

Figure 1. Schematic overview of the development of the daily air temperature gridded dataset (PISCOt). Input data, related processes, and main output files are specified. Spatial interpolation uses the Regression Kriging (RK) and Geographically Weighted Regression Kriging (GWRK) techniques.

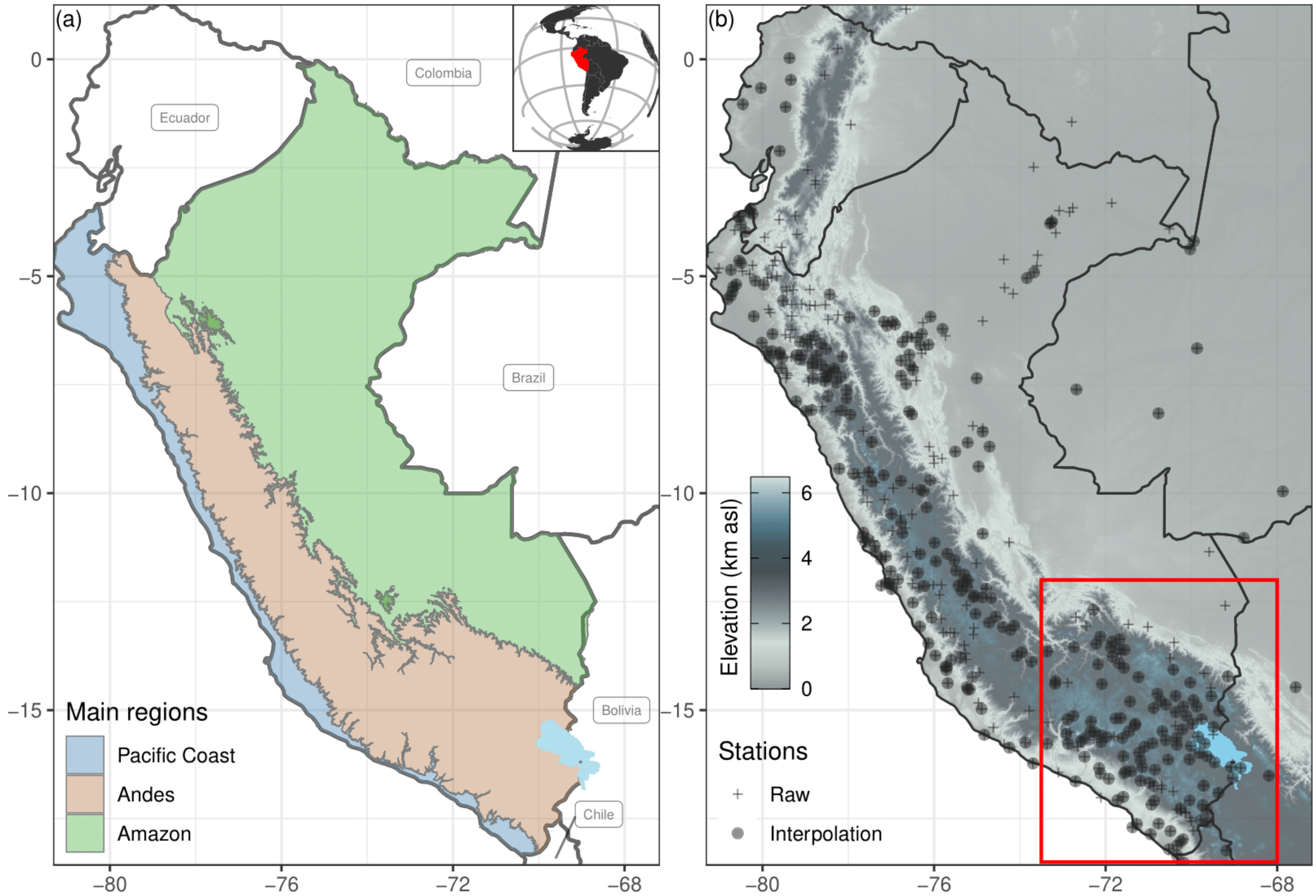

Figure 2. (a) Study area of Peru and its three main regions: Pacific Coast, Andes, and Amazon. The panel in the upper right corner shows the location of the study area in South America. (b) Spatial distribution of 462 available time series (Raw) for daily maximum (Tmax) and minimum (Tmin) temperature. After the data pre-processing, 302 time series were used for spatial interpolation (Interpolation). The red box represents the southern Andes of Peru. Water bodies (area > 10 km^2) are shown in light blue.

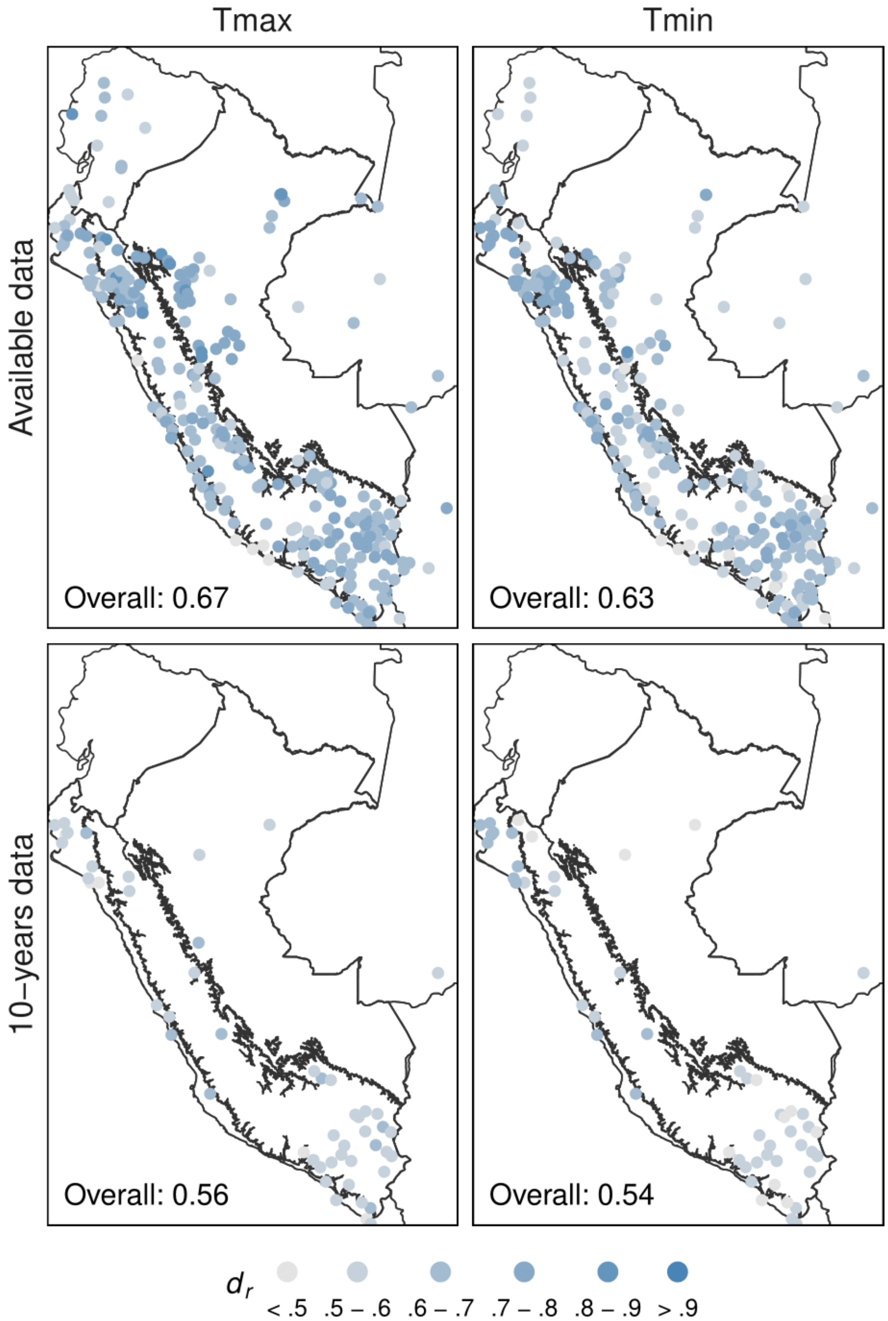

Figure 3. Spatial distribution of the refined index of agreement (d_r) for gap filling (1981-2020) of daily maximum (Tmax) and minimum (Tmin) air temperature for data available during the entire study period and for at least a 10-year window within that period (with $\geq 75\%$ data). Black lines represent the three main climate regions: Pacific Coast (Western Peru), Andes (Central Peru), and Amazon (Eastern Peru).

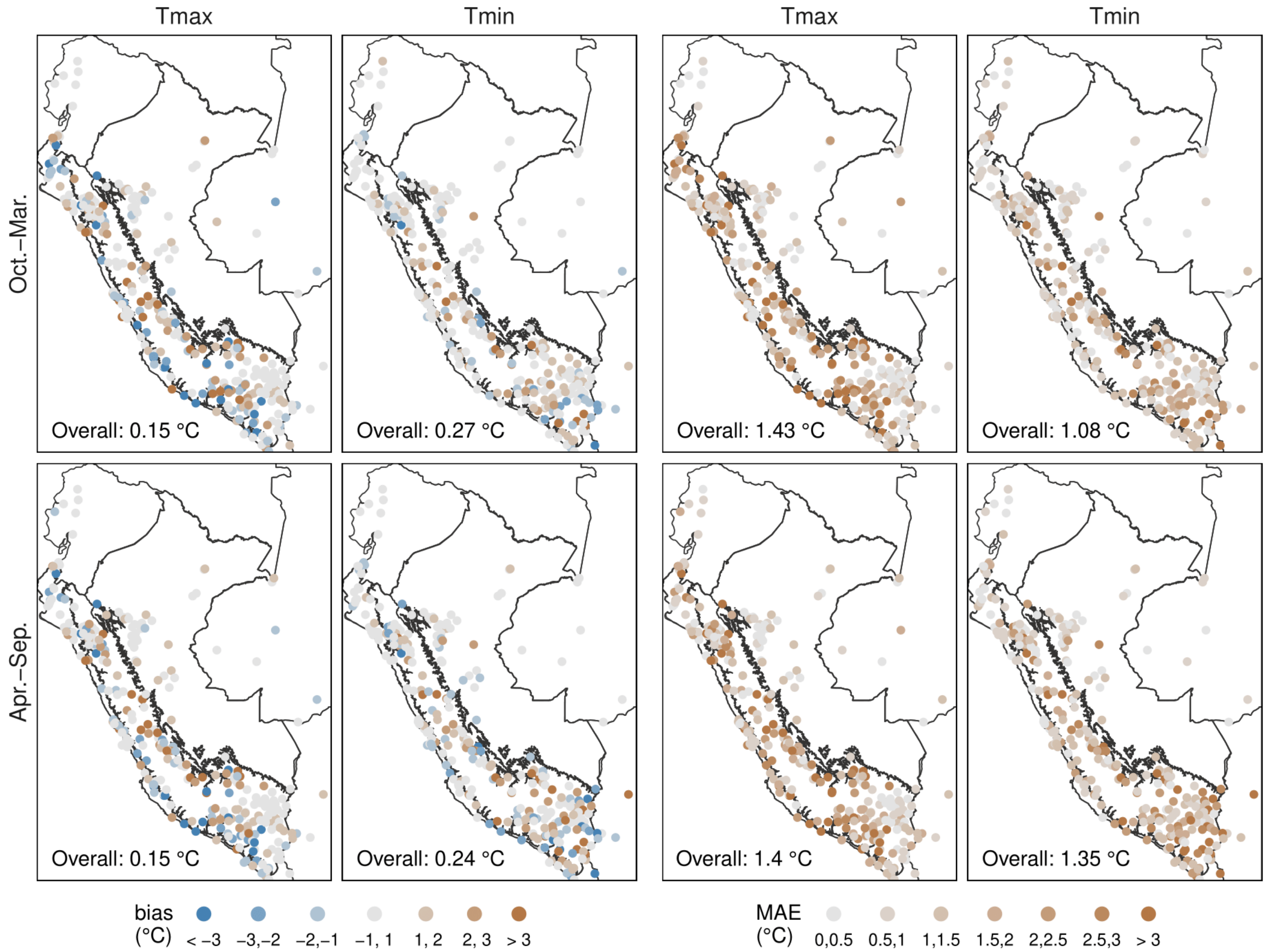

Figure 4. 10-fold cross-validation bias and mean absolute error (MAE) for interpolated monthly maximum (Tmax) and minimum (Tmin) normal temperature in the period 1981-2010 (n = 299 stations). Black lines represent the three main climate regions in Peru (Fig. 3)

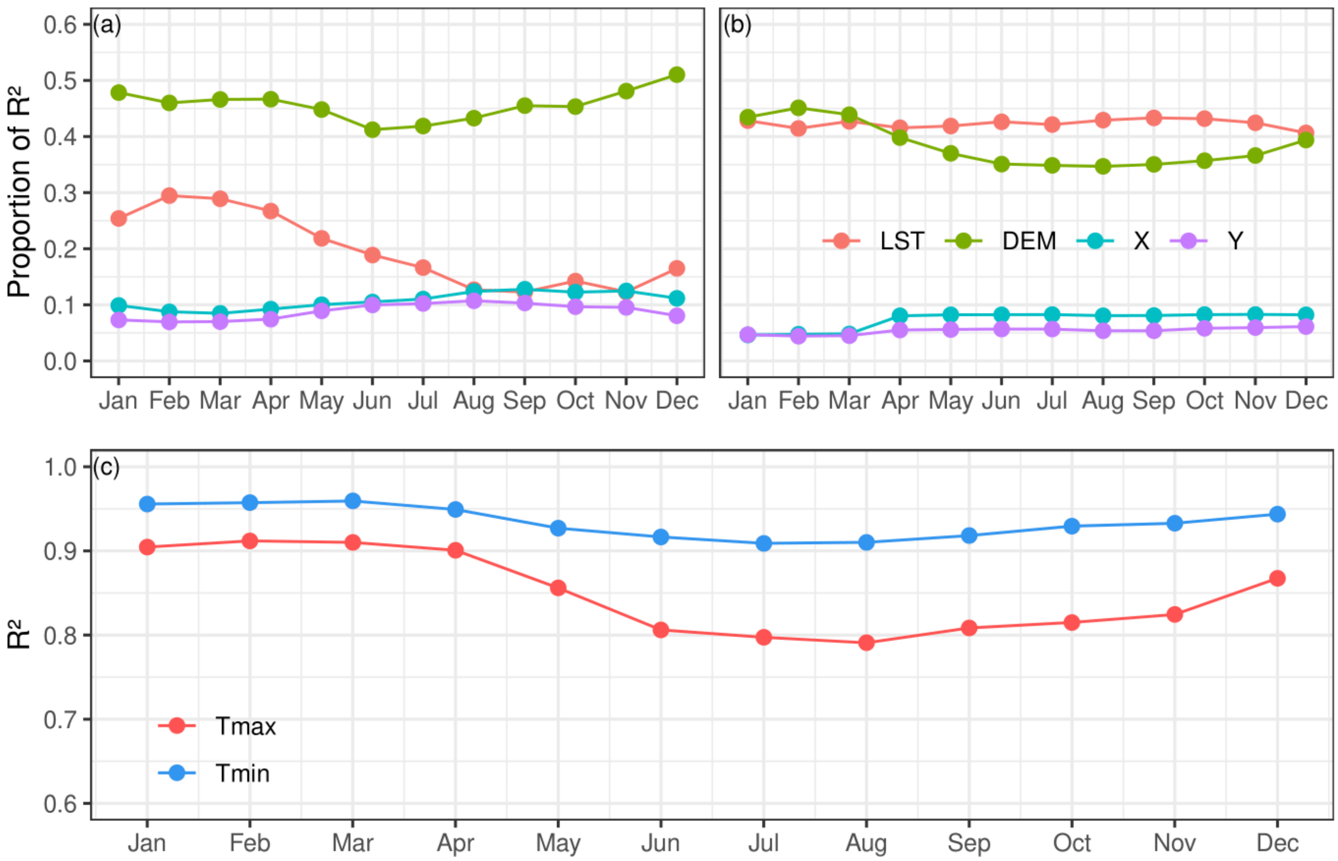

Figure 5. Relative and absolute influence of spatial predictors (land surface temperature (LST), elevation (DEM), latitude (Y), and longitude (X)) over Peru using a monthly-normal moving window with multiple linear regression relating the Geographically Weighted Regression Kriging (GWRK). Proportion of variance explained (R^2) of each predictor for (a) maximum air temperature (Tmax) and (b) minimum air temperature (Tmin); and, (c) overall R^2. The statistical values are averaged over 253 stations.

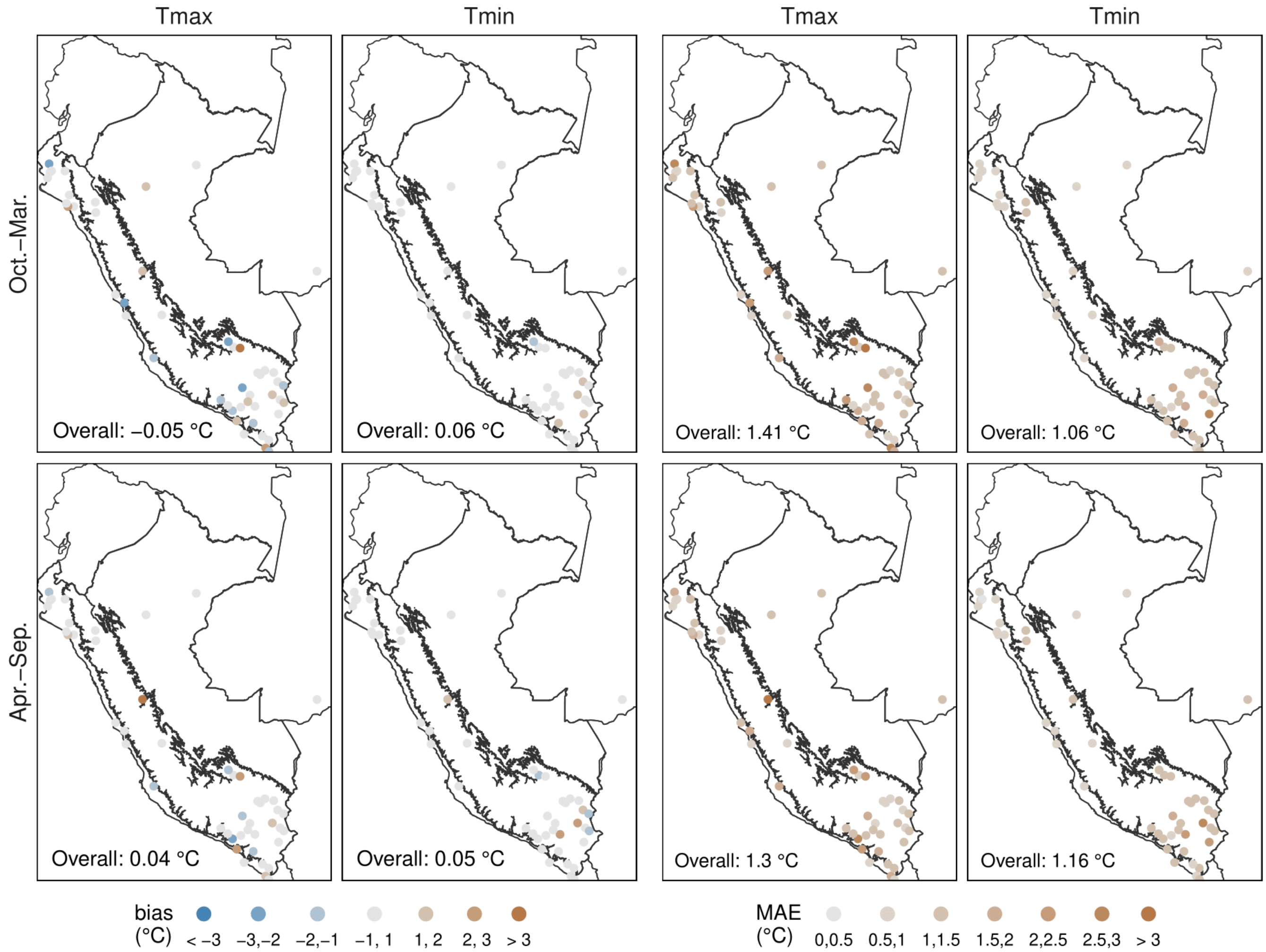

Figure 6. 10-fold cross-validation bias and mean absolute error (MAE) for interpolated daily maximum (Tmax) and minimum (Tmin) temperature in the period 1981-2010 (n = 48 stations). Black lines represent the three main climate regions in Peru (Fig. 3)

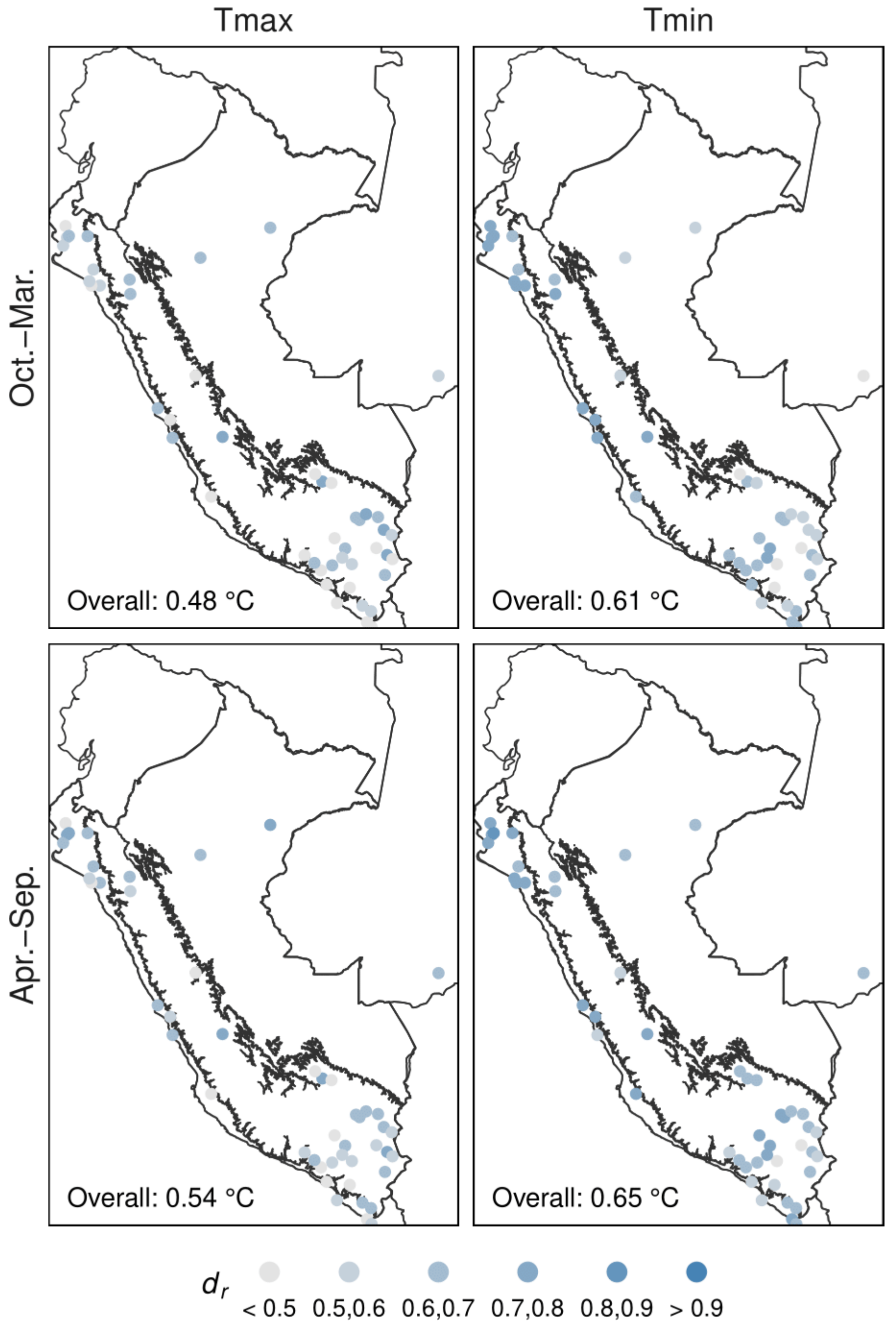

Figure 7. 10-fold cross-validation refined index of agreement (d_r) for interpolated daily maximum (Tmax) and minimum (Tmin) temperature in the period 1981-2010 ($n = 48$ stations). Black lines represent the three main climate regions in Peru (Fig. 3).

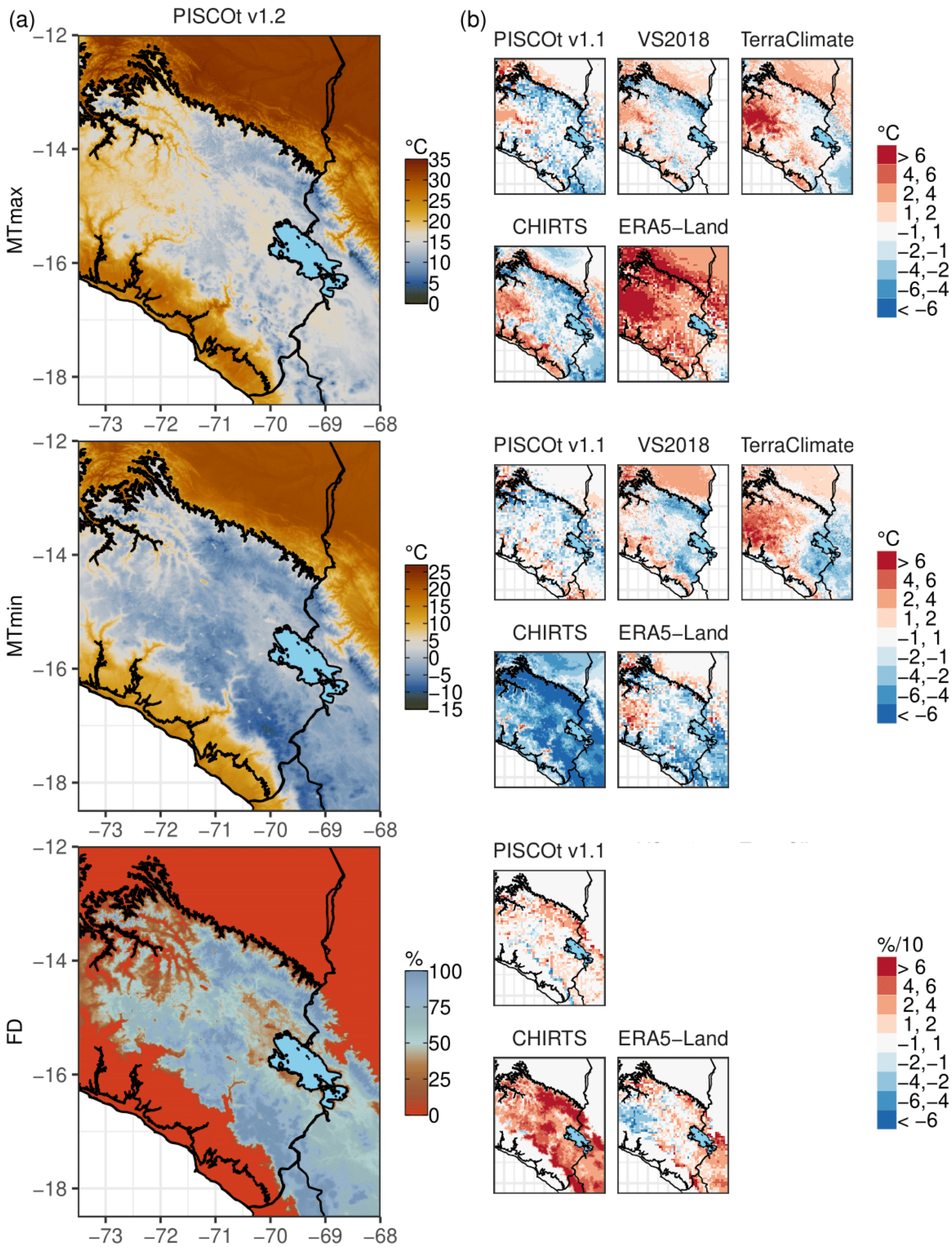

Figure 8. Spatial distribution and differences of the mean annual (1981-2010) temperature indices (mean Tmax (MTmax), mean Tmin (MTmin), and frost days (FD)) in the southern Andes of Peru. (a) Spatial distribution for PISCOt v1.2. (b) Difference of PISCOt v1.2 with each gridded product (PISCOt v1.1, VS2018, TerraClimate, CHIRTS, and ERA5-Land) and temperature indices. For CHIRTS, the mean average corresponds to 1983-2010. Black lines represent the three main climate regions in Peru (Fig. 3); Lake Titicaca is shown as a lightblue filled area.

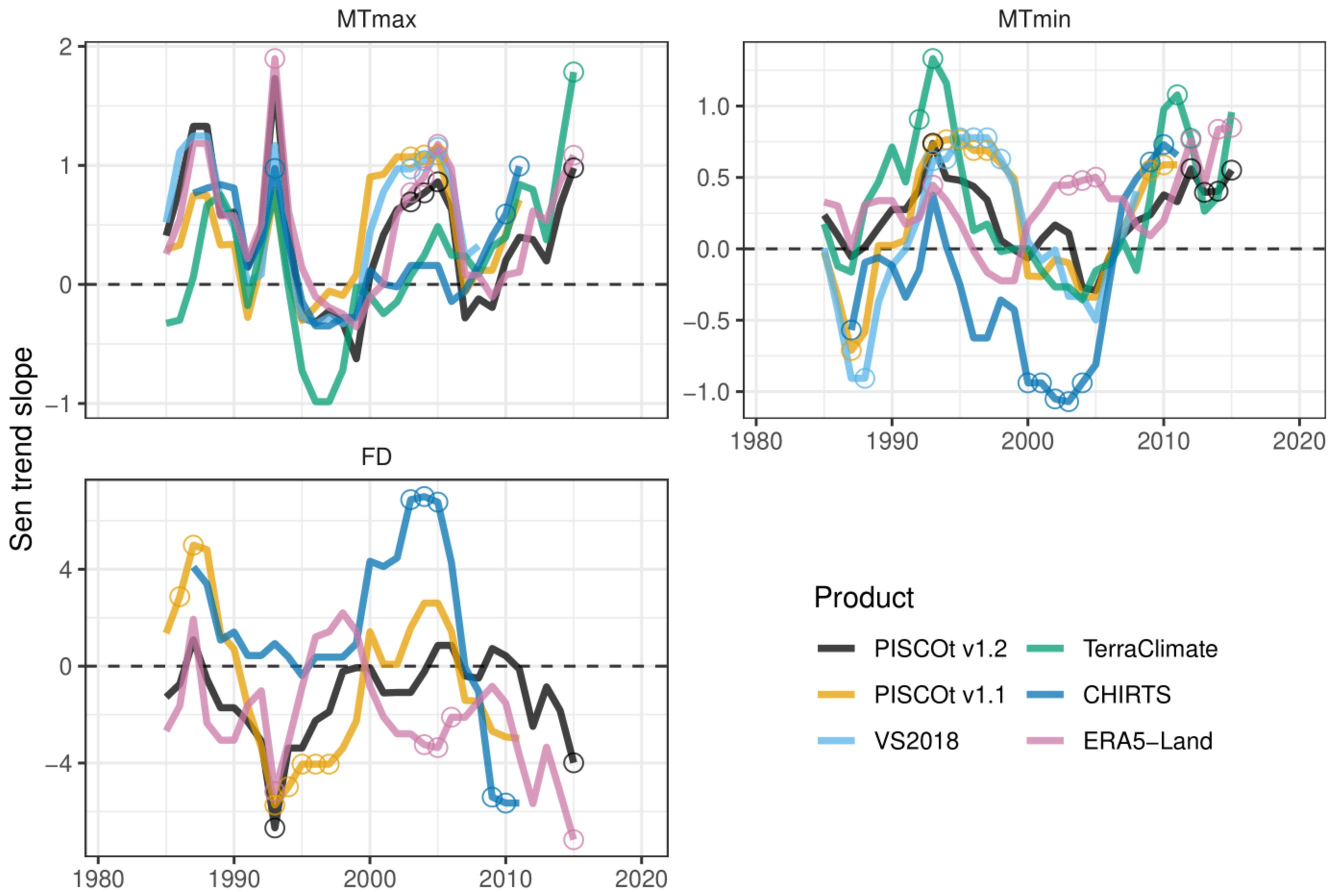

Figure 9. Running annual Sen's slope (for 10-years window from 1981 to 2020) of temperature indices (mean Tmax (MTmax), mean Tmin (MTmin), and frost days (FD)) for PISCOt v1.2 and gridded products (PISCOt v1.1, VS2018, TerraClimate, CHIRTS, and ERA5-Land) in the southern Andes of Peru (following delimitation of red box in Fig. 2 considering all land > 2000 masl). Significant trend estimates (Mann–Kendall trend test with $p < 0.05$) are shown with an open circle. The x-axis shows the centroid year of running trends.

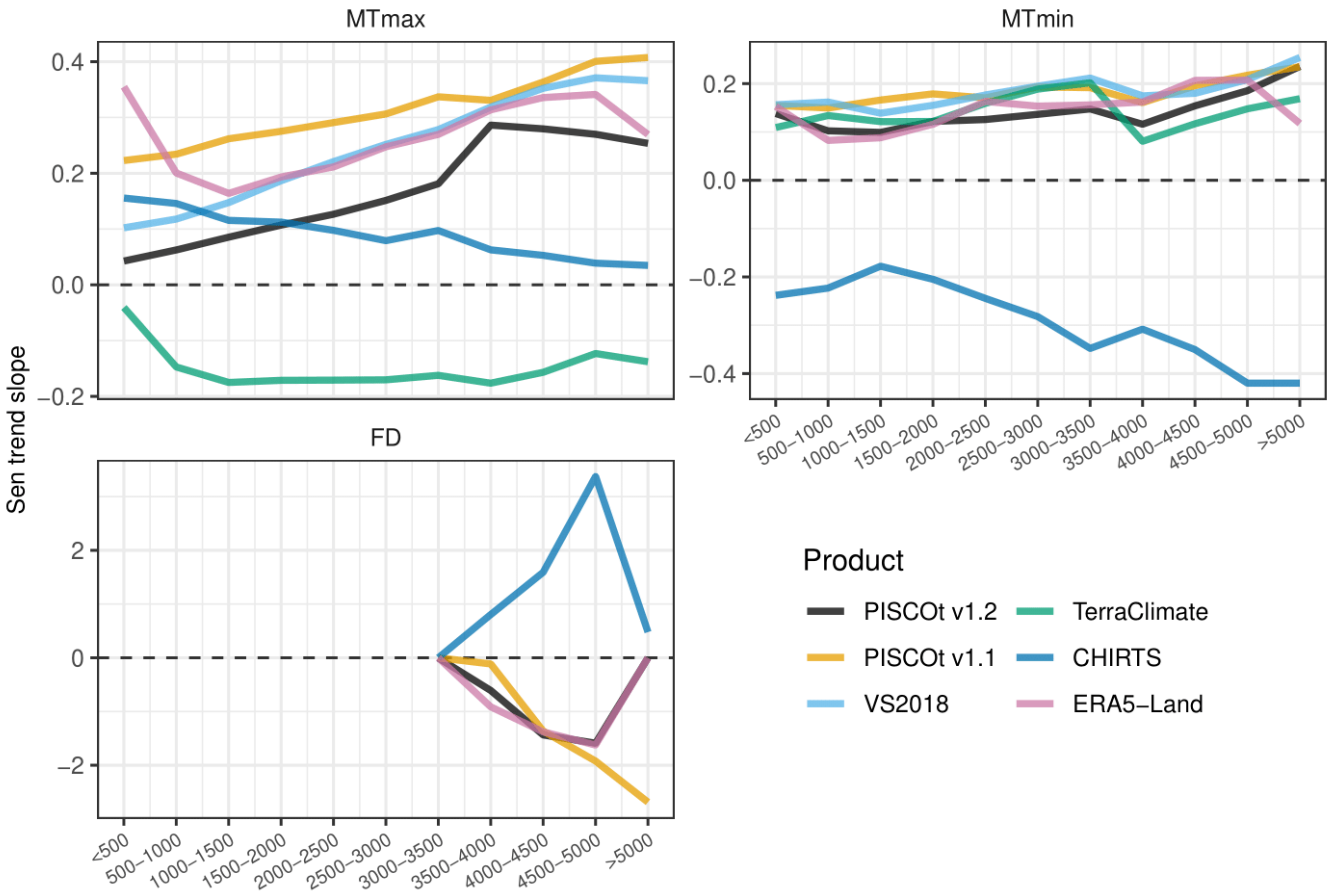

Figure 10. Annual Sen's slope (1983-2013) of temperature indices (mean Tmax (MTmax), mean Tmin (MTmin), and frost days (FD)) per different elevations intervals (km asl.) for PISCOt v1.2 and gridded products (PISCOt v1.1, VS2018, TerraClimate, CHIRTS, and ERA5-Land) over the southern Andes of Peru.

Experiment	Tmax				Tmin			
	Number of stations	bias (°C)	MAE (°C)	d_r	Number of stations	bias (°C)	MAE (°C)	d_r
Available data	346	0.11	0.98	0.67	342	0.1	0.98	0.63
10-years data	51	0.03	1.27	0.56	52	-0.02	1.44	0.54

Table 1. Gap filling error statistics for daily maximum (Tmax) and minimum (Tmin) temperature for bias, mean absolute error (MAE) and refined index of agreement (dr) for (1981-2020) using all available data and when only a complete period of 10-years (with $\geq$ 75% data) is available.